

An Inner-Shelf Wave Forecasting System for the U.S. Pacific Northwest

GABRIEL GARCÍA-MEDINA

School of Civil and Construction Engineering, Oregon State University, Corvallis, Oregon

H. TUBA ÖZKAN-HALLER AND PETER RUGGIERO

College of Earth, Ocean and Atmospheric Sciences, Oregon State University, Corvallis, Oregon

JEFFREY OSKAMP

School of Civil and Construction Engineering, Oregon State University, Corvallis, Oregon

(Manuscript received 4 June 2012, in final form 10 January 2013)

ABSTRACT

An operational inner-shelf wave forecasting system was implemented for the Oregon and southwest Washington coast in the U.S. Pacific Northwest (PNW). High-resolution wave forecasts are useful for navigational planning, identifying wave energy resources, providing information for site-specific coastal flood models, and having an informed recreational beach user group, among other things. This forecasting model is run once a day at 1200 UTC producing 84-h forecasts. A series of nested grids with increasing resolution shoreward are implemented to achieve a 30-arc-second resolution at the shelf level. This resolution is significantly higher than what the current operational models produce, thus improving the ability to quantify the alongshore variations of wave conditions on the PNW coast. Normalized root-mean-squared errors in significant wave height and mean wave period range from 0.13 to 0.24 and from 0.13 to 0.26, respectively. Visualization of the forecasts is made available online and is presently being used by recreational beach users and the scientific community. A series of simulations, taking advantage of having a validated shelf-scale numerical wave model, suggests that neither dissipation due to bottom friction nor wind generation is important in the region at this scale for wave forecasting and hindcasting when considering bulk parameters as opposed to the processes of refraction and shoaling. The Astoria and McArthur Canyons; the Stonewall, Perpetua, and Heceta Banks; and Cape Blanco are significant bathymetric features that are shown to be capable of producing alongshore variability of wave heights on the shelf.

1. Introduction

An increasing interest in understanding the ocean waves in the Pacific Northwest (PNW) region of the United States has been fueled by an observed multi-decadal increase in wave heights (Allan and Komar 2000, 2006; Komar et al. 2009; Menéndez et al. 2008; Ruggiero et al. 2010; Seymour 2011; Young et al. 2011), the potential for harvesting wave energy in the region (Arinaga and Cheung 2012; Cornett 2009), and the need to make localized, informed decisions in an evolving climate, such as coastal flood warnings. As waves propagate from deep water to inner-shelf regions [with water depths of $O(20)$ m],

they are affected by the underwater topography (bathymetry). The West Coast shelf is characterized by a complex shelf bathymetry with numerous canyons, large banks, capes, and headlands. These features may focus, divert, and transform wave energy by the processes of refraction, shoaling, diffraction, and dissipation due to bottom friction and wave breaking. Inner-shelf wave predictions need to resolve the relevant bathymetric features and account for the associated wave transformation processes.

The National Oceanic and Atmospheric Administration's (NOAA) National Weather Service (NWS) operates a third-generation wave forecasting model called WAVEWATCH III. This model contains the necessary physics to account for shelf-scale wave transformation processes if the bathymetry at the relevant length scales is defined. However, the current forecasts in the eastern

Corresponding author address: Gabriel García-Medina, 104 CEOAS Administration Bldg., Corvallis, OR 97331.
E-mail: ggarcia@coas.oregonstate.edu

North Pacific Ocean are produced at a resolution of 15 arc minutes (19.8 km in the cross-shore direction and 27.8 km in the alongshore direction at 44.5°N). At this resolution, there are only 17 computational nodes along Oregon's coast, and bathymetric features along the coast cannot be adequately resolved. Further, due to this coarse resolution, the grid cell that is closest to the shore may be in water depths of as much as 315 m, failing to specify the wave field in the inner-shelf region. Hence, the current forecasting system may not be capable of capturing the alongshore variability of wave conditions necessary for site-specific purposes.

To satisfy a range of needs in the PNW, a high-resolution wave forecasting model was implemented for the Oregon and southwest Washington coast using the WAVEWATCH III version 3.14 (v3.14) numerical model (Tolman 2002b). This operational forecasting model provides 84-h forecasts at a 30-arc-second resolution. At this resolution the model provides 510 output points along the Oregon coastline and enables the generation of a high-resolution wave climate database. The forecasting system is forced by wind fields and air-sea temperature differences generated by NOAA's National Centers for Environmental Prediction (NCEP). In this paper, we describe the implementation of the wave forecasting model for the PNW. The operational aspects of the forecast are also described, and model validation with available shelf-scale wave observations is carried out. We then take advantage of the validated numerical wave model and investigate the dominant wave transformation processes in the region. The importance of including dissipation due to bottom friction and wind generation at the shelf scale is assessed by performing a series of numerical simulations including and neglecting these physical processes. Further, at this high resolution we are able to capture the effect of large-scale bathymetric features such as canyons, banks, capes, and headlands. Therefore, we investigate the effect of these features on the inner-shelf wave field making use of two numerical wave models, WAVEWATCH III v3.14 and Simulating Waves Nearshore (SWAN) v40.81 (Booij et al. 1999; SWAN Team 2010).

2. The Pacific Northwest

The PNW region, Oregon and Washington, receives hundreds of thousands of visitors yearly that include, but are not limited to, recreational beach users and surfers. For instance, shore-based whale watching accounts for more than 126 000 visitors each year in Oregon (Christensen et al. 2007). There are important commercial ports in Astoria and Newport, and in general Oregon experiences high boat traffic activity. The region

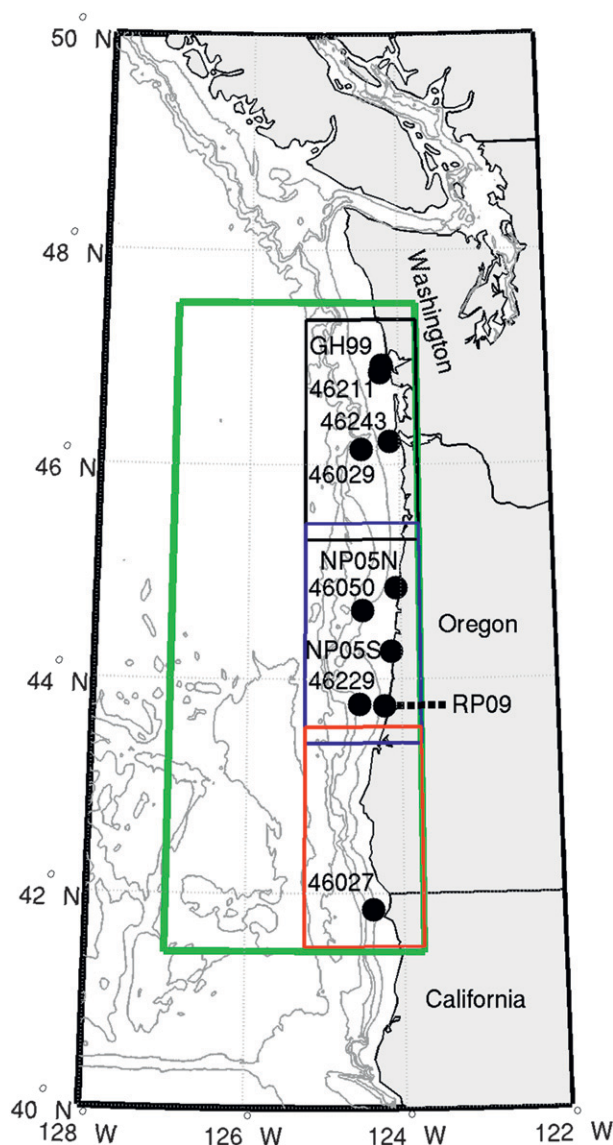


FIG. 1. Model domain. This figure shows the locations (dots) of the data sources used in this study. The outer grid is boxed in green, the northern shelf grid in black, the central shelf grid in blue, and the southern shelf grid in red. Contours are at 100-, 250-, 500-, 1000-, and 3000-m depths.

of interest for our study extends more than 420 km from north to south (see Fig. 1). The region's shelf is characterized by multiple complex bathymetric features. These include the Astoria, Willapa, Guide, and McArthur Canyons; the Stonewall, Siltcoos, Perpetua, and Heceta Banks; and multiple capes and headlands.

Waves in the PNW vary throughout the year and along the coast. The wave climate in this region is characterized by large wave heights in the winter months. Approximately one event per year exceeds significant wave heights (SWHs) of 10 m (Ruggiero et al. 2010).

TABLE 1. Average wave statistics at buoy 46050 recorded from 1991 to 2009. Winter is considered to span October–March.

Time period	SWH (m)	PWP (s)	PWD (°)
Annual	2.4	10.8	282
Winter	3.0	12.2	273
Summer	1.8	9.5	289

The strongest storms recorded in the region have generated offshore SWHs of approximately 15 m (Allan and Komar 2006). Table 1 shows average wave conditions from a record spanning from 1991 to 2009 (inclusive) at National Data Buoy Center (NDBC) buoy 46050 (see Fig. 1).¹ This buoy is located 37 km offshore in 128 m of water. Waves are generally higher in the winter than in the summer. They also tend to be longer in the winter; this indicates that these waves are produced far from the measuring location. Figure 2 shows measured wave data for 2009. During this particular year the maximum wave height reached 9.3 m. Further, waves in this region approach from various directions throughout the year, although in general waves tend to come from the northwest during the Northern Hemisphere's summer and from the west during the winter.

A multidecadal increase in SWH in this region has been well documented during the previous and present decades (Allan and Komar 2000, 2006; Komar et al. 2009; Menéndez et al. 2008; Ruggiero et al. 2010; Seymour 2011; Young et al. 2011). Ruggiero et al. (2010) evaluated wave buoy data and reported that the average winter SWH has increased annually at a rate of 0.023 m yr^{-1} . This same report suggests that the rate of increase for the annual maximum SWH is even higher. Gemmrich et al. (2011) found a relatively limited wave height increase and pointed out problems with buoy data prior to 1985. Young et al. (2011) studied the world's wave climate using altimeter data from 1985 to 2008 and found that the 99th percentile SWH shows a positive trend in the northeastern Pacific Ocean. Larger waves are a concern because they result in an increase in the dangers associated with ocean-related activities. Identifying the reasons and implications of SWH increases is currently the subject of active research, and assessing possible links between increasing nearshore SWHs and changing wind conditions can be aided by the use of a shelf-scale

wave forecasting system for the region. Another purpose of implementing a high-resolution wave forecasting model is that alongshore variable wave data will be available in advance to coastal modelers interested in high-resolution coastal flood forecasting. During extreme events in the PNW, the wave runup, which is a function of wave height, has been the main contributor to the total water levels along the coast (Allan and Komar 2002). Hence, localized predictions for flood risk in coastal communities require a high-resolution prediction of inner-shelf wave height.

The highly energetic waves off the coasts of Oregon and Washington are also well suited for wave energy harvesting (Arinaga and Cheung 2012; Cornett 2009). Many emerging wave energy harvesting technologies are designed to operate in the inner shelf with water depths of less than 40 m (Falcão 2010). However, most of the long-term observations on this coast are from wave buoys in much deeper water, and there is indication that, at some locations, wave power can be reduced more than 20% when waves approach the nearshore from deep water (Folley and Whittaker 2009); therefore, a shelf-scale wave-energy characterization is desired. Due to high costs, obtaining long-term wave data in intermediate waters at a high spatial resolution along the PNW is not viable. A validated shelf-scale wave forecasting system is well suited to provide wave information in these regions. This information can then be used to identify possible sites for wave energy harvesting. Wave forecasts can also inform computations of the near-future energy yield of an installed device for device-tuning purposes.

3. Numerical model

The WAVEWATCH III v3.14 (WW3; Tolman 2002b) is the numerical model implemented in this project. This is a third-generation phase-averaged wave model developed by NCEP that solves the spectral wave action balance equation:

$$\frac{\partial N}{\partial t} + \frac{\partial(c_{gx} + U_x)N}{\partial x} + \frac{\partial(c_{gy} + U_y)N}{\partial y} + \frac{\partial c_\theta N}{\partial \theta} + \frac{\partial c_\omega N}{\partial \omega} = \frac{1}{\sigma}(S_{in} + S_{ds} + S_{nl} + S_{bf} + S_{brk}) \quad \text{and} \quad (1)$$

$$\omega = \sigma + \mathbf{k} \cdot \mathbf{U}, \quad (2)$$

where $N \equiv E/\sigma$ is the wave action for a component and is a function of frequency (ω), direction (θ), time (t) and position (x, y); σ is the relative radian frequency; ω is the absolute radian frequency; $\mathbf{U} = (U_x, U_y)$ is the depth- and time-averaged current velocity vector; $\mathbf{k} = (k_x, k_y)$ is

¹ Oceanographic convention will be used throughout this discussion. Under this convention the direction from which waves are approaching is measured clockwise from true north. Thus, waves approaching from the west are said to have an angle of incidence of 270° .

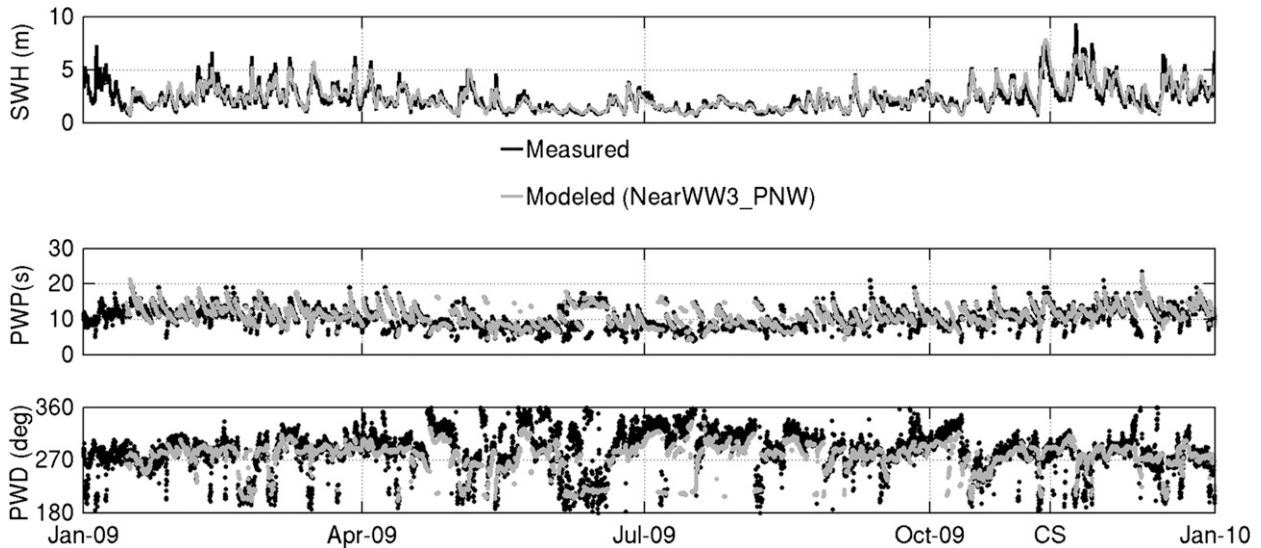


FIG. 2. The 2009 wave conditions at buoy 46050 near Newport: (from top to bottom) SWH, PWP, and PWD. The PWD is the direction from which the waves approach, where 360° indicates waves are traveling from the north. The first 2 weeks of model spinup were excluded from the plot. CS marks the dates of the discussed “case studies” in section 5b.

the wavenumber vector with a magnitude k equal to $(2\pi/L)$, L being the wavelength; and h is the water depth. The left-hand side of Eq. (1) accounts for the linear propagation of the wave component, the first term represents the local rate of change of wave action, while the next four terms represent the advection of wave action in the x , y , θ , and ω dimensions, respectively. The group velocities (c_{gx} , c_{gy}) determine the velocity at which wave action travels in the horizontal plane by

$$\mathbf{c}_g = \frac{\partial \sigma}{\partial \mathbf{k}} \quad (3)$$

Energy propagation in the wavenumber space (c_θ), representing the process of refraction, is given by

$$c_\theta = -\frac{1}{k} \left(\frac{\partial \sigma}{\partial h} \frac{\partial h}{\partial n} + \mathbf{k} \cdot \frac{\partial \mathbf{U}}{\partial s} \right), \quad (4)$$

where n and s are the coordinates perpendicular to and in the direction of wave propagation. Energy propagation in the frequency space (c_ω) is represented as

$$c_\omega = \frac{\partial \sigma}{\partial h} \frac{\partial h}{\partial t} + \mathbf{k} \cdot \frac{\partial \mathbf{U}}{\partial t}. \quad (5)$$

On the right-hand side of Eq. (1), S_{in} and S_{ds} represent the input and dissipation of energy due to wind and whitecapping, respectively. In this implementation WW3 defaults based on an atmospheric boundary layer formulation are used (Tolman and Chalikov 1996). Also, S_{nl} are the nonlinear quadruplet wave interactions, modeled

using the discrete interaction approximation (Hasselmann et al. 1985) and S_{bf} is the dissipation by bottom friction represented by the linear Joint North Sea Wave Project (JONSWAP) formulation (Hasselmann et al. 1973). The default value for the bottom friction coefficient ($\Gamma = 0.067 \text{ m}^2 \text{ s}^{-3}$) was used. The quantity S_{brk} represents dissipation of energy due to depth-induced breaking modeled with the Battjes and Janssen (1978) approach. The default values for the wave breaking coefficient ($\gamma = 0.73$) and the intensity of breaking ($\alpha = 1$) were also used. Finally, the frequency and wavenumber are related by the dispersion equation:

$$\sigma^2 = gk \tanh(kh). \quad (6)$$

These equations are solved with a third-order explicit propagation scheme (Booij and Holthuijsen 1987) that includes a scheme to alleviate the garden sprinkler effect (Tolman 2002a). The wave spectrum was discretized in direction with 24 bins spaced at 15° and in frequency with 25 bins using a logarithmic spacing from 0.041 18 to 0.5 Hz.

a. Model implementation

The proposed implementation (hereafter referred to as NearWW3_PNW) is built taking advantage of WAVEWATCH III v3.14's mosaic nesting capabilities (Tolman 2006, 2008). Having multiple nested grids focuses the computational resources where they are needed. Waves in intermediate to shallow waters are affected by the bathymetry; therefore, higher resolution

is needed as waves approach the shore. In this implementation four levels are part of the mosaic. To account for wave generation at oceanic scales, we use in-house versions of models based on NCEP's global and eastern North Pacific (ENP) grids, making up two levels of nesting. The global grid provides near-global coverage at $1.25^\circ \times 1.00^\circ$ resolution, in the latitudinal and longitudinal directions, respectively. It covers a region from 77°S to 77°N . With 15-arc-minute resolution, the ENP covers a region from 5° to 60.25°N and from 170° to 77.5°W .

To account for local bathymetric features on the Oregon continental shelf, we then assembled a grid (referred to as the outer grid) with 3-arc-minute resolution in both the latitudinal and longitudinal directions. This grid covers a region from 41.45° to 47.50°N and from 127° to 123.75°W (see Fig. 1). The shallowest grid cell at the deep water boundary is at 2090 m. The outer grid interacts with three highly resolved "shelf" grids that have resolutions of 30 arc seconds in both the latitudinal and longitudinal directions. These grid points are spaced 927 m apart in the alongshore direction, resulting in 510 cells along the Oregon coast. In the cross-shelf direction the grid spacing varies from 694 to 627 m, depending on the latitude. The combination of the three shelf grids covers a region from 125.25° to 123.75°W . The southern grid covers a region from 41.50° to 43.55°N (see Fig. 1). The central one covers a region from 43.40° to 45.45°N . The northern grid goes from 45.30° to 47.35°N . In summary, there are six grids in a four-level mosaic.

The bathymetry data for the outer and shelf grids were obtained from NOAA's National Geophysical Data Center (NGDC). In 2006 the NGDC started building high-resolution digital elevation models (DEMs) along the U.S. coast (Carignan et al. 2009a–d; Grothe et al. 2010, 2011). This dataset was chosen because these DEMs carefully incorporate many available public surveys, coastline databases, and lidar surveys. Their resolution along the West Coast is $\frac{1}{3}$ arc second. The western boundaries of these DEMs do not always extend to deep water; therefore, they were combined with 1-minute gridded topography–bathymetry from the ETOPO1 global relief model (Amante and Eakins 2009).

Finally, the implementation of a wave forecasting model requires atmospheric data in order to force the model. The operational forecasting model developed herein is driven by wind fields at 10-m elevation above the water surface produced by the Global Forecasting System (GFS) as atmospheric input (Sela 1980; Environmental Modeling Center 2003). The GFS is executed 4 times a day (0000, 0600, 1200, and 1800 UTC) by the NCEP. The current model (version 9.1.0) has a horizontal resolution of roughly $\frac{1}{2}^\circ$ in both the latitudinal and longitudinal

directions. To account for boundary layer stratification, air and sea temperatures are obtained from NCEP's Global Data Assimilation System (GDAS). The air–sea temperature difference is computed and, along with the wind fields, is used to determine the wave growth with the Tolman and Chalikov (1996) source terms. The wind fields that force the wave model act on all grids, and linear interpolation in time and space is used to apply them at every time step and grid cell. At this moment, NearWW3_PNW neglects ocean and wave-driven currents. In addition, results in water depths shallower than 20 m, which we consider the inner-shelf's inner limit, are masked out of the output products.

b. Operational wave forecasting

NearWW3_PNW has been operational since May 2011. At the time of this writing, the model is executed twice a day. The first model run is aimed at updating the initial conditions for the forecasting model. This first run is initiated at 1300 UTC on any given day and involves an 18-h hindcast for the conditions between TAU 24 and TAU 6. Note that wave hindcasting is the prediction of waves based upon past analyzed meteorological and oceanographic data (Rao and Mandal 2005), so the hindcast involves higher quality input and forcing data than the forecasts. The model run then continues with a short-range 6-h forecast until TAU 00. For this run, GDAS-analyzed, 3- and 6-h forecasted winds, and air–sea temperature differences from the last four NOAA runs are used to force the model. This model run, therefore, performs a 24-h computation with higher quality input and forcing.

Starting from the estimated conditions for TAU 00, we then perform a wave forecast with a TAU +84-h horizon. For the wave forecasting model, wind forecasts are downloaded from the GFS ftp server at 1610 UTC, and the forecasting model is initiated immediately. Currently, the model runs on 44 threads on two UNIX servers that have two six-core Intel Xeon CPUs clocking at 2.7 GHz. The forecasts are completed around 0100 UTC of the next day, and forecasts for nearly 3 days (~ 71 h) become available at that time. Spectral output is being produced at the locations of buoys 46211, 46243, 46029, 46050, 46229, and 46027 (see Fig. 1), as well as at a site in 40 m of water depth near Reedsport, Oregon, and along the 25-m contour at 2-km intervals. Bulk wave parameters are stored at every grid cell and are made available upon request in the World Meteorological Organization's Gridded Binary (GRIB1) format.

c. Wave hindcasting

NearWW3_PNW can also be executed in hindcast mode. Hindcasts are performed to validate the model

TABLE 2. Short-term wave data sources. The ADP stands for acoustic Doppler profiler. Water depth is reported relative to mean sea level.

Identifier	Depth (m)	Operation	Location	System
RP09	40	Autumn 2009	Offshore Reedsport, OR	AWAC
NP05	13–15	Summer 2005	Offshore Newport, OR	AWAC
GH99	22–25	Autumn 1999	Offshore Grays Harbor, WA	ADP and pressure sensor

with in situ measurements that were gathered in the past. Wind forcing for these simulations comes from the NOAA/NCEP GFS reanalysis; in other words, these are analyzed wind fields instead of forecasted, therefore resulting in higher quality input. Consequently, hindcast performance most closely characterizes errors in the wave model physics; forecast errors could be higher than these because of compounding errors associated with the wind forecasts. To validate NearWW3_PNW, three hindcasts were performed: during autumn 2009, summer 2005, and autumn 1999. These times were selected based on the availability of ground truth data as explained in section 4a.

4. Model accuracy

To validate this implementation, model data are compared against in situ data. To quantify the performance of NearWW3_PNW, root-mean-squared error (RMSE), normalized root-mean-squared error (NRMSE), the scatter index (SI), bias, and the linear correlation coefficient (r^2) will be used throughout the discussion. Details regarding the definition of these metrics are described in the appendix.

a. Data sources

We compared model results with available in situ wave data within the region covered by our high-resolution domains. We had access to intermediate to shallow water wave data collected during three field experiments. These are described in Table 2 and experiment locations are shown in Fig. 1. Both the RP09 and NP05 deployments used Acoustic Wave and Current Sensors (AWAC) to measure wave activity. These sensors track the water surface and particle velocity, and these data were converted to wave spectral information by making use of linear wave theory. The RP09 deployment covered a period from 18 September to 2 December 2009. During this deployment the average SWH, peak wave period (PWP, calculated from the 1D frequency spectrum using a parabolic fit around the discrete peak), and peak wave direction (PWD, calculated from the 1D direction spectrum in the same fashion as PWP) were 2.5 m, 11.1 s, and 291°, respectively. The maximum recorded SWH during this experiment was 6.8 m while the longest PWP was 19.9 s.

The NP05 data consist of an initial deployment (NP05S) near Newport, Oregon, at 15-m water depth from 15 June to 13 July 2005 [for a complete description of the data collection from this experiment, the reader is referred to Kirincich et al. (2009)]. During the deployment time the instrument recorded average SWHs, PWPs, and PWDs of 1.3 m, 8.5 s, and 284°, respectively. The maximum recorded SWH was 4.0 m. A second deployment (NP05N) took place north of the first one at 13-m water depth from 23 July to 22 September 2005. During the deployment time the instrument recorded average SWHs, PWPs, and PWDs of 1.3 m, 8.9 s, and 281°, respectively. The maximum recorded SWH was 3.4 m.

The GH99 data were collected as part of the Grays Harbor Wave Refraction Experiment of 1999 (Gelfenbaum et al. 2000). Wave information was collected using a pressure sensor that recorded pressure fluctuations. Spectral wave data for surface elevation were generated using linear wave theory. We considered data from two stations from this experiment: ND and SD.² ND was located northwest of Ocean Shores, Washington, and occupied twice, from 1 October to 2 November 1999 at 23-m water depth and from 5 November to 29 December 1999 at 25-m water depth. The SD station was located south of ND near Westport, Washington. It was also occupied twice at 22-m water depth from 2 October to 27 November 1999 and from 27 November to 29 December 1999. During the deployment time ND registered average SWHs and mean wave periods (MWP) of 3.3 m and 11.3 s, respectively.³ Throughout, this discussion MWP will be used to refer to $T_{m01}(=2\pi m_0/m_1)$, where $m_n = \int \omega^n S(\omega) d\omega$ and $S(\omega)$ is the variance frequency spectrum. The integration was performed from 0.041 18 to 0.5 Hz without considering a parametric tail. This experiment was performed during a very energetic time, with four events exceeding SWHs of 7 m and a maximum event of 9.7 m.

Since the model provides shelf-scale coverage, data from buoys located in the region were also considered.

² In this article, we use the same nomenclature that was used to refer to these locations in Gelfenbaum et al. (2000).

³ Only significant wave height and mean wave period data were distributed.

TABLE 3. Long-term wave data sources. Water depth is reported relative to mean sea level.

Buoy identifier	Depth (m)	Operation since	Location	System
46029	135	1984	37 km west of MCR at OR–WA border	3-m Discus
46050	128	1991	37 km west of Newport, OR	3-m Discus
46229	187	2005	Offshore Umpqua, OR	Waverider
46211	38	2004	Offshore Grays Harbor, WA	Waverider
46243	25	2009	Clatsop Spit, OR	Waverider
46027	48	1983	15 km west-northwest of Crescent City, CA	3-m Discus

These are long-term deployments maintained by NDBC or the Coastal Data Information Program (CDIP) from the Scripps Institution of Oceanography in La Jolla, California. Table 3 shows details on the nature and location of these buoys, which are mapped in Fig. 1. These buoys undergo periodic maintenance and are sometimes damaged and go out of operation during severe weather conditions; therefore, the data are not always continuous. For this study only quality controlled data were used to evaluate the performance of the model [for more information on the quality controls performed by NDBC the reader is referred to NDBC (2009)].

b. Hindcast and forecast performance

To assess hindcast performance, a total of three hindcasts were performed. These cover the period of the wave data available from the field experiments and analyzed wind fields. Two hindcasts covered roughly 3 months each, one from September to November 2009 and the other from mid-June to mid-September 2005, and a third hindcast covered the months of November

and December 1999 (see Table 2). Model agreement with available buoy data during these same hindcast periods was also evaluated. The performance statistics are summarized in Table 4. For all of the performed hindcasts, the predicted SWH is highly correlated with observations ($r^2 > 0.82$); this is consistent with existing high-resolution localized wave forecasting systems (Alvarez-Ellacuria et al. 2010). For autumn 2009 and summer 2005, the RMSEs range from 0.20 to 0.57 m resulting in percent errors in wave height (NRMSE) of 13%–23%. The largest errors in the SWH predictions occur for the 1999 hindcast (up to 0.88 m, or 24%, errors), and this may be due to the difference in quality of the wind fields. The GFS model has been updated numerous times over the last decade, including resolution increases and additional physics, among other things, and the analyzed winds for 1999 are likely less accurate than those for 2005 and 2009. Nevertheless, even with inferior wind forcing the model still shows a good level of agreement, resulting in high correlation coefficients. Biases are smaller for the autumn 2009 hindcast, and

TABLE 4. The NearWW3_PNW validation table. Here, N is the number of observations, RMSE is the root-mean-squared error (m), NRMSE is the normalized root-mean-squared error, SI is the scatter index, and r^2 is the linear correlation coefficient. For the 1999 and 2005 hindcasts, only the high-resolution shelf grid that included the short-term deployment was used. All three high-resolution shelf grids were used in the autumn 2009 hindcast. Mean wave period data were not available for 26229 during the summer 2005 hindcast.

Hindcasted period	Buoy	N	Depth (m)	Significant wave height					Mean wave period				
				RMSE (m)	NRMSE	SI	Bias (m)	r^2	RMSE (s)	NRMSE	SI	Bias (s)	r^2
Autumn 2009	RP09	1729	40	0.50	0.21	0.20	0.19	0.93	1.07	0.16	0.13	0.62	0.86
	46229	2555	189	0.48	0.19	0.19	0.08	0.93	1.16	0.18	0.15	0.77	0.87
	46050	2511	123	0.45	0.18	0.18	0.11	0.94	0.90	0.13	0.11	0.48	0.89
	46243	661	25	0.57	0.17	0.17	−0.01	0.91	1.28	0.23	0.15	0.64	0.78
	46029	2565	135	0.44	0.16	0.17	0.06	0.95	0.91	0.14	0.11	0.44	0.88
	46211	2496	38	0.49	0.20	0.21	0.06	0.92	1.18	0.19	0.15	0.69	0.81
Summer 2005	46027	2481	48	0.53	0.23	0.22	0.02	0.87	0.96	0.13	0.12	0.60	0.89
	NP05N	1477	13	0.20	0.13	0.15	−0.05	0.92	1.10	0.18	0.18	0.92	0.88
	NP05S	667	15	0.27	0.17	0.21	−0.01	0.82	1.28	0.22	0.21	1.11	0.69
	46229	2280	189	0.45	0.20	0.25	−0.28	0.87	—	—	—	—	—
November 1999	46050	2593	123	0.40	0.19	0.23	−0.25	0.89	1.04	0.18	0.16	0.65	0.77
	ND	1310	25	0.88	0.20	0.24	−0.54	0.86	3.40	0.24	0.28	−2.31	0.57
	SD	751	22	0.85	0.20	0.24	−0.50	0.88	3.53	0.24	0.29	−2.33	0.53
October 1999	ND	772	23	0.65	0.24	0.26	−0.38	0.92	2.37	0.20	0.23	−1.31	0.59
	SD	1127	22	0.76	0.22	0.26	−0.38	0.88	2.41	0.26	0.24	−1.13	0.47

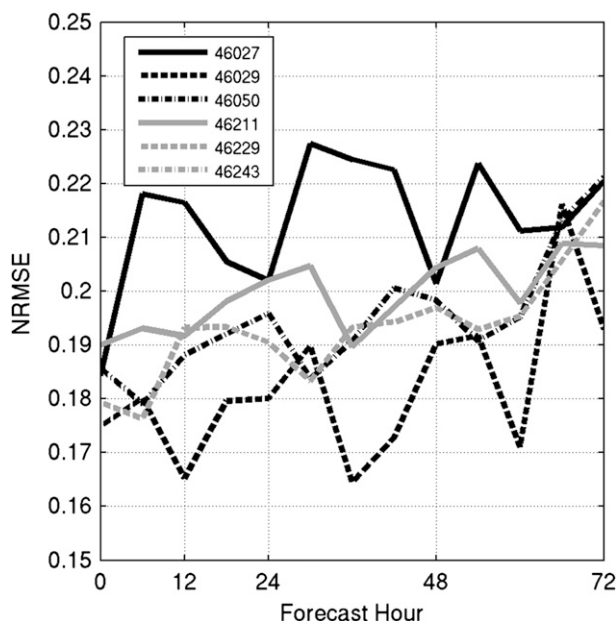


FIG. 3. The NearWW3_PNW NRMSEs of significant wave height at selected buoy locations as a function of forecast hour from October to December 2011.

large negative biases (indicating underprediction) are present for the 1999 hindcast [\sim (from -0.4 to -0.5) m]. The MWP is predicted with ~ 1.1 -s error for the 2009 and 2005 datasets. Errors for the 1999 datasets are about twice as large, with the bias indicating underprediction. Correlation values for the MWP are not as high as those associated with the SWH predictions for the 1999 and 2005 hindcasts but are similar in the 2009 hindcast.

Forecast accuracy can be characterized by comparing the forecasts at different TAUs with the actual measured conditions. Figure 3 shows NRMSE in SWH as a function of forecast hour for the six NDBC or CDIP buoys in our region of interest from October to December 2011 when the average SWH, PWP, and PWD at buoy 46050 were 2.9 m, 12.0 s, and 282° , respectively. As expected,

forecast accuracy is similar to the hindcast accuracy at TAU 00 [\sim (17%–19%)], but then declines slightly with forecast hour. This decline is a function of the forcing uncertainty since the wind forecast error increases with forecast time as well. However, the forecast accuracy decreases only by a few percentage points [to \sim (19%–22%)] over 72 h. Hence, NearWW3_PNW produces accurate forecasts even at the 72-h horizon.

c. Seasonal performance

To assess the possibility of a seasonal trend in model performance, a 4-yr hindcast was performed including the global, ENP, and outer domains from 2007 to 2010. The SWH prediction was evaluated by monthly averaging the NRMSE and bias metrics for the deeper water buoys 46229, 46050, and 46029. Since these buoys are located in relatively deep water, the shelf grids were not included in the hindcast. Results are plotted in Fig. 4 for these three buoys; discontinuities are due to the absence of measured data. Examination of the bias metric indicates that the SWH is often overpredicted. The bias shows larger errors during the winter months similar to what Hanson et al. (2009) reported. However, this is also when wave heights are larger. The NRMSE metric does not show an appreciable seasonal trend. The errors are also uncorrelated among these buoys; seasonal trends in normalized metrics are not dominant.

d. Comparison with the existing operational model

NearWW3_PNW provides over 600 points along the Oregon and Washington coast, capturing the distinctive alongshore bathymetric features of the region and taking them into account for the wave forecasts. The left panel in Fig. 5 shows the SWH interpolated to the 250-m contour along the modeling domain for both NearWW3_PNW and the NCEP ENP model. Discontinuities in the ENP line exist because at 42.75°N the shallowest grid point of the ENP model is at 315-m water

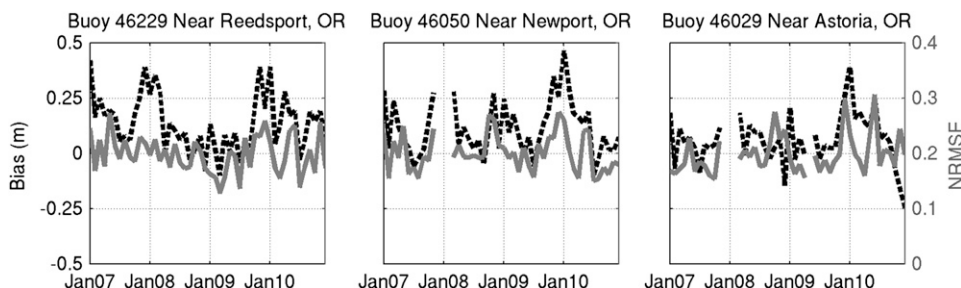


FIG. 4. The NearWW3_PNW seasonal performance at (left to right) selected buoys. Bias and NRMSE in significant wave height are represented by the black dashed and gray solid lines, respectively. All reported values are averaged over a month from a 4-yr hindcast.

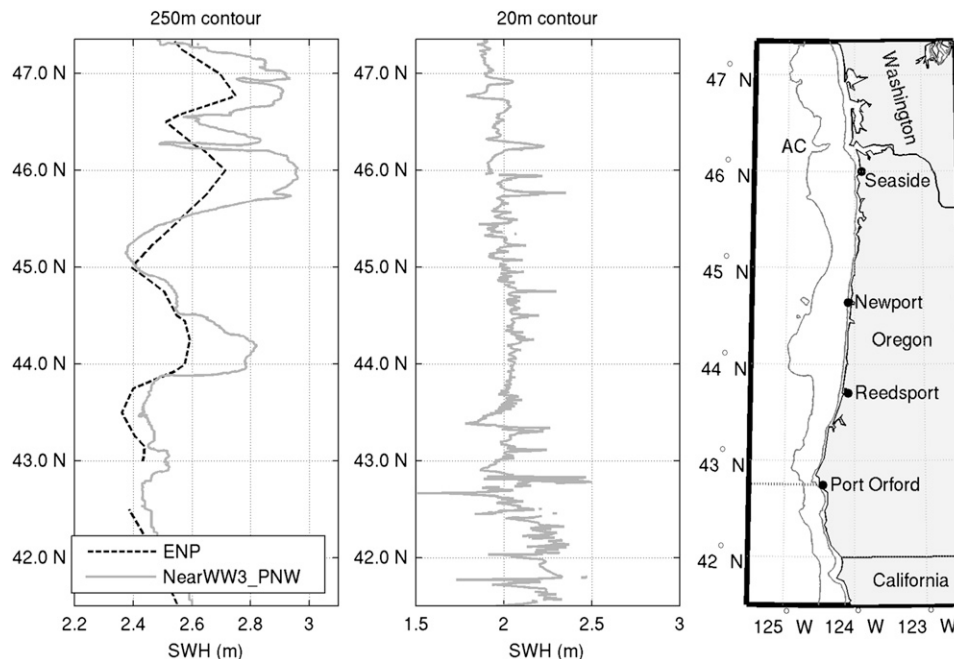


FIG. 5. (left) Significant wave height interpolated at the 250-m contour from both the NearWW3_PNW and NCEP ENP. (middle) Significant wave height interpolated at the 20-m contour. (right) Map of the coast of the study area with contour lines at 20- and 250-m water depths. These are forecasted results for 1200 UTC 26 Sep 2012. Without considering the estuaries, the average distance between the 20-m contour and the coast is 2.1 km. The dotted line at 42.75°N shows the location of the transect for which results are shown in Fig. 7; AC stands for Astoria Canyon.

depth. The higher resolution allows for the representation of features such as the Astoria Canyon. Canyons divert wave energy by the process of refraction, thus reducing the wave energy density. This is shown as a reduction in the wave height near 46.25°N, the effect of the canyon in the inner-shelf wave field is discussed in section 5b(2). The middle panel in Fig. 5 shows SWH interpolated at the 20-m contour from both operational models. NearWW3_PNW provides nearly complete coverage of this region. At 20-m water depth, the proposed implementation has 99% active points while the ENP model has 4% (see Fig. 6). This metric is based on all potential wet points outside of the land contour for each model latitude as a function of water depth. At any transect, the shallowest active grid point is considered. If it is located in shallower depth than the evaluated depth contour, the model is considered to have an active point at that transect. The percentage of active transect is reported for each depth in Fig. 6. This improved resolution is important for coastal flood warnings because modern empirical formulations for wave runup are based on local SWH at approximately 20-m water depth (Stockdon et al. 2006).

As previously mentioned, many emerging wave energy devices are intended to be deployed in shallow

water. To estimate the expected power output, wave forecasts are needed where the wave energy device is located. Figure 7 shows forecasted SWH along 42.75°N by the NCEP ENP model and NearWW3_PNW. The current operational model is incapable of resolving the wave field in the inner shelf and does not provide any data in some regions. NearWW3_PNW provides data up to the 20-m contour, capturing the wave transformations

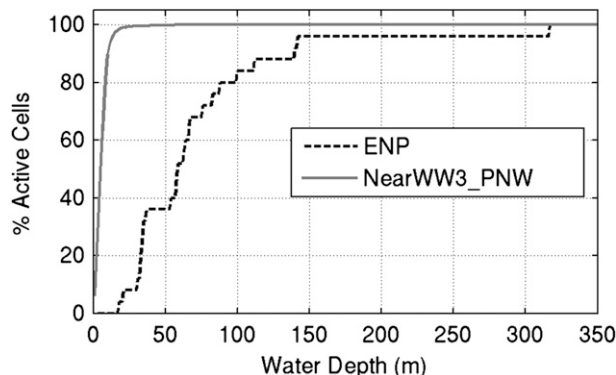


FIG. 6. Percentage of alongshore active cells in each model as a function of depth. Only the first active cell in each grid latitude was considered to compute this metric. The ENP has 25 points while NearWW3_PNW has 722 points in the study area.

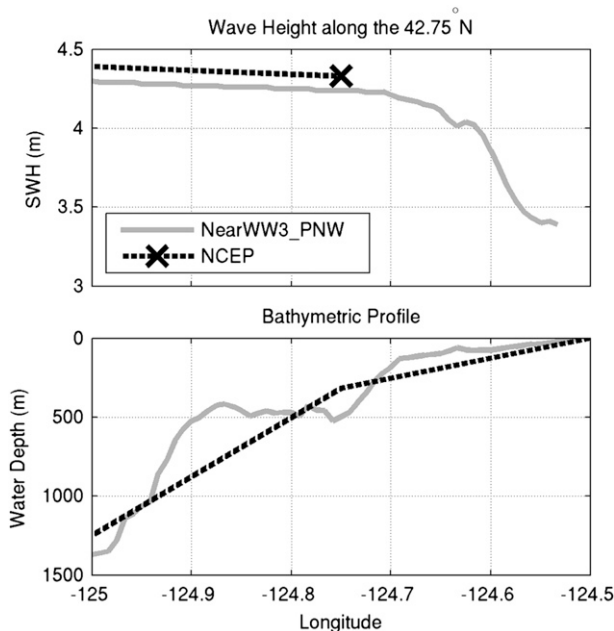


FIG. 7. (top) The significant wave height along 42.75°N. Forecast data from NCEP and NearPNW_WW3 were used to generate this plot. The NCEP model does not give any information for water depths shallower than 300 m at this latitude while NearPNW_WW3 provides data up to the 20-m contour. (bottom) The bathymetries used by the two different models. These are forecasted results for 1200 UTC 29 Sep 2011, where the offshore MWP and MWD were 11 s and 290°, respectively.

due to the topography at the shelf scale. Thus, both implementations are complementary: one providing open-ocean forecasts and NearWW3_PNW providing shelf-scale coverage.

5. Dominant wave transformation processes

Taking advantage of the assembled and validated wave forecasting model along the entire Oregon and the southwest Washington coast, we investigate the effects of isolated physical processes in the region. First, we will analyze the importance of bottom friction and wind input over the continental shelf. For this purpose in situ shallow water ground truth data were compared to a series of simulations where these physics were omitted. Further, we investigate the effects of refraction over bathymetric features on the continental shelf by studying test cases in which the nearshore wave field is altered by offshore features. For these the NearWW3_PNW hindcasts were complemented with simulations from a different numerical model, SWAN (see section 5b).

a. Effect of bottom friction dissipation and wind input

The PNW region is characterized by a relatively narrow continental shelf, with length scales on the order of

~15 to ~60 km (0.2° – 0.8°). This raises the question of the relative importance of including bottom friction and wind forcing at the shelf scale. To evaluate this, a series of one-way nested hindcasts were performed for the RP09 and NP05 data (see section 4b). One-way nesting was selected in order to completely isolate the shelf-level grids from those that produced the boundary conditions. First, a WAVEWATCH simulation consisting of a mosaic of our three lower-resolution models (global, ENP, and outer) was executed. Wave spectra were stored for each hindcast hour from the outer model at 3-arc-minute resolution around the open boundaries of the three shelf grids. These low-resolution hindcasts include all the physics used for the validation runs and the operational forecasts with the exception of the stability correction for wind growth, as described by Tolman (2002b). Exclusion of this correction translates into smaller wave heights, which becomes evident when comparing these results with the validation data.

The SWH was computed from the different hindcasts at the location of the in situ data and the time series were compared by computing the performance metrics described in the appendix; the results are summarized in Table 5. In general, there are no appreciable differences when comparing the time series generated by each model execution. The model performance is not significantly affected regardless of the considered physics, suggesting that neither bottom friction nor wind growth are important at the shelf scale for wave forecasting–hindcasting in the PNW and likely in locations with similar shelf characteristics. Only the bias metric is slightly affected; both cases that exclude wind wave generation show a larger negative bias than those that include it. The simulations that excluded the winds also excluded whitecapping, the process responsible for steepness-limited wave breaking dissipation. An additional simulation was performed that neglected wind input but included whitecapping dissipation for the NP05S station. Wave heights at this station show a larger negative bias than do the other cases, meaning that whitecapping is responsible for the observed reduction in the wave energy. Thus, whitecapping has a bigger impact than wind generation in these locations. Nevertheless, the differences are on the order of 5 cm. It is worth mentioning that our analysis does not include the surf zone, where depth-limited wave breaking is expected to be the dominant dissipation mechanism.

b. Effect of wave refraction over bathymetric features

In this section we investigate the effect of large-scale bathymetric features on the shallow water wave field in

TABLE 5. Friction and wind input effect. Inclusion of physical process in the model run is marked by an X. RMSE, NRMSE, SI, bias, and r^2 are computed for significant wave height at the location of three AWAC deployments. Refer to the appendix for details on how these metrics are computed.

Hindcasted period	Buoy	Wind	Friction	Whitecapping	N	RMSE (m)	NRMSE —	SI —	Bias (m)	r^2 —
Autumn 2009	RP09	X	X	X	1424	0.52	0.22	0.23	−0.30	0.91
						0.52	0.22	0.23	−0.24	0.90
			X			0.52	0.22	0.23	−0.25	0.90
				X		0.52	0.22	0.23	−0.29	0.91
Summer 2005	NP05N	X	X	X	1477	0.46	0.31	0.35	−0.39	0.87
						0.43	0.29	0.33	−0.35	0.86
			X			0.44	0.30	0.34	−0.37	0.86
				X		0.44	0.30	0.34	−0.37	0.87
	NP05S	X	X	X	667	0.47	0.29	0.36	−0.35	0.75
						0.45	0.27	0.34	−0.31	0.73
			X			0.45	0.28	0.35	−0.32	0.73
				X		0.46	0.28	0.35	−0.34	0.75
			X	X		0.48	0.30	0.37	−0.36	0.73

the PNW. From the hindcasts described in section 4b, we identified three interesting sets of features; they are the Stonewall, Heceta, and Perpetua Banks; the Astoria and Willapa Canyons; and Cape Arago and Cape Blanco. In the following subsections we will evaluate wave transformation processes near these features. First, we will identify cases where wave modifications due to the features of interest are evident.

Our simulations show that the banks have the ability to focus energy in certain locations shoreward. During the autumn of 2009 there were several events where waves had peak periods in excess of 10 s. For example, 7 November 2009 conditions (shown in Fig. 8) indicate the possibility of waves focusing shoreward of the Heceta Bank (right panel). Wave height is focused at certain locations offshore from the area between Newport and Reedsport with north–south scales from $\sim 0.2^\circ$ to $\sim 0.5^\circ$. However, when examining the wave field at the 20-m contour (left panel), there is no clear evidence of variations at the scales of the wave focusing. The wave height at the 20-m isobath responds to shallower bathymetric effects with smaller length scales (less than $\sim 0.2^\circ$). Hence, we investigate under which, if any, conditions the waves at the 20-m contour can contain alongshore variability at length scales related to the banks. Being interested in large-scale behavior in this discussion, we introduced a running average to smooth the SWH plots on a contour; its effect is shown in Figs. 8–10 (as well as Fig. 12). The large-scale variations are preserved by the smoothing while the small-scale signals are eliminated. This averaging replaces all SWH values with the average value of a specified stencil; in the remaining graphs where we plot SWH at a contour, the stencil width varies from 11 to 15 points with the replaced value in the center.

In our northern domain, the bathymetry is radically different. Instead of being dominated by banks, it is dominated by canyons. Contrary to banks, these divert wave energy. When evaluating our hindcasts, strong alongshore gradients in wave height were identified at the 20-m isobath in the northern coast of Oregon and the southwest coast of Washington. Figure 9 shows results from the autumn 2009 Hindcast at this location for the 7 November 2009 conditions when long waves approached from the northwest. Several focusing and defocusing regions are evident and are associated with the canyons, especially the Astoria and Willapa canyons.

In southern Oregon, the shoreline shows a change in orientation near Cape Blanco. Results from the autumn 2009 hindcast near Reedsport indicate lower wave height regions to the north of Cape Blanco and Cape Arago when waves approached at angles of less than 225° (from the southwest). Figure 10 shows the results for 2300 UTC 5 November 200, when this effect is evident.

All example cases discussed above show a decrease in the wave height shoreward of the 150-m contour, even in areas with nearly straight and parallel contours. Several potential processes can give rise to such a decrease. Bottom friction or other dissipation processes may be at play; however, analysis in the previous section showed that these processes affect the predicted wave height minimally on this shelf. Refraction of obliquely incident waves (even over straight and parallel contours) is another process that could cause a sustained decrease in the wave height with decreasing water depth since the wave energy is distributed over a longer wave crest as the wave refracts toward shore (see Dean and Dalrymple 1991). Finally, the group velocity of waves shows a small increase as waves first start feeling the presence of the bottom before the monotonic decrease as water depth

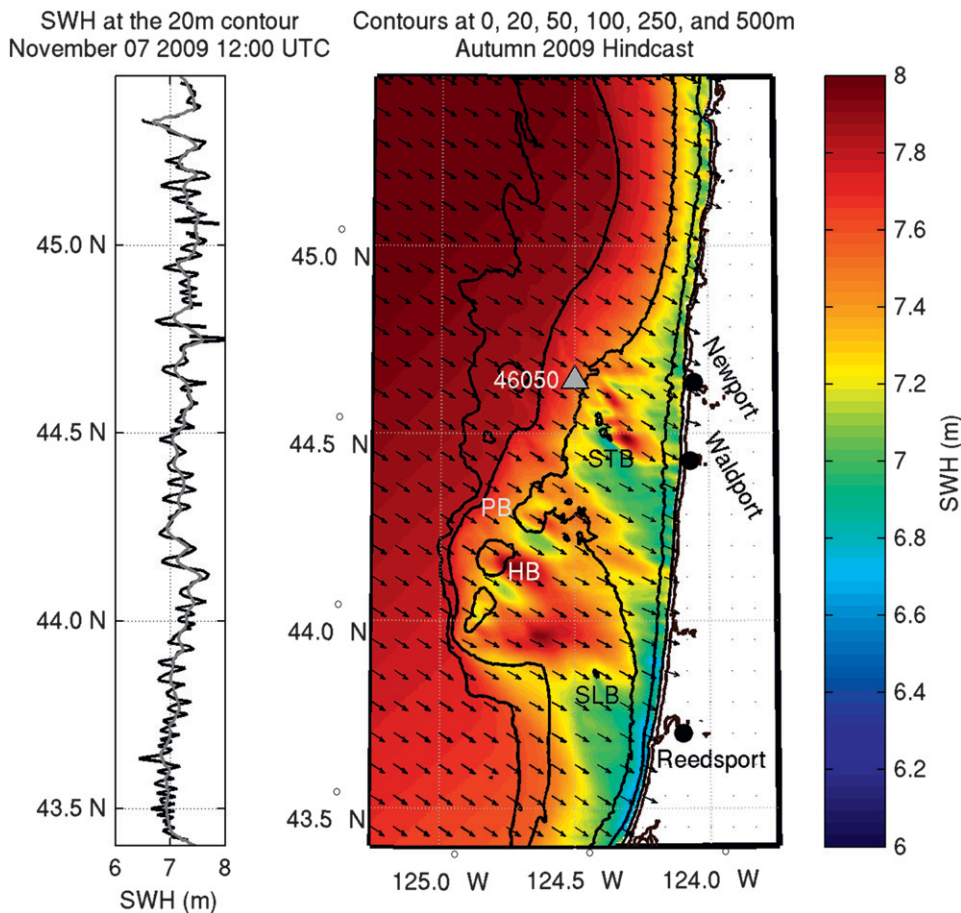


FIG. 8. Spatial variations of SWH from the autumn 2009 NearWW3_PNW hindcast with wave focusing due to the banks offshore of the central OR region. (left) SWH at the 20-m contour (black) and smoothed using a running average (gray). (right) The NearWW3_PNW results at the shelf level. Waves at water depths shallower than 20 m are masked in the color plot. At buoy 46050 the modeled SWH was 7.6 m with mean wave period of 16.3 s and peak wave direction of 293°. The banks are identified as STB for Stonewall Banks, PB for Perpetua Bank, HB for Heceta Bank, and SLB for Siltcoos Bank.

decreases further. Conservation of energy flux dictates that the wave shoaling process will then result in a decrease in wave height before a sustained increase in wave height with decreasing depth. This behavior is predicted by linear wave theory and has been observed in the laboratory (Iversen 1952).

All cases also show alongshore variability in wave conditions that appear to be linked to the identified banks, canyons, and capes. However, temporal and spatial variability associated with arriving storms can also induce alongshore variability in the inner shelf even in the absence of any bathymetric features. To isolate the effect of bathymetry on wave transformation processes (i.e., refraction and shoaling) while eliminating possible effects related to the variability of the offshore wave field, we perform a series of idealized simulations using the wave transformation model SWAN, which

allows for alongshore-uniform conditions at the offshore boundary and the determination of a steady-state solution.

The third-generation phase-averaged spectral wave model SWAN is a well-established wave propagation and transformation model that, similar to WAVEWATCH III v3.14, solves the action balance equation. SWAN has been proven skillful in simulating waves over the complex West Coast bathymetry (Gorrell et al. 2011; Rogers et al. 2007). By implementing this model in our domain, a careful evaluation of the effects of the aforementioned features can be accomplished. Whenever SWAN simulations were used, the model was run in steady-state mode [$\partial N / \partial t = 0$ in Eq. (1)] and no source or sink terms other than depth-limited wave breaking dissipation were considered (e.g., wind input, whitecapping dissipation, quadruplets, bottom friction). Wave breaking was estimated with the Battjes and Janssen (1978) approach

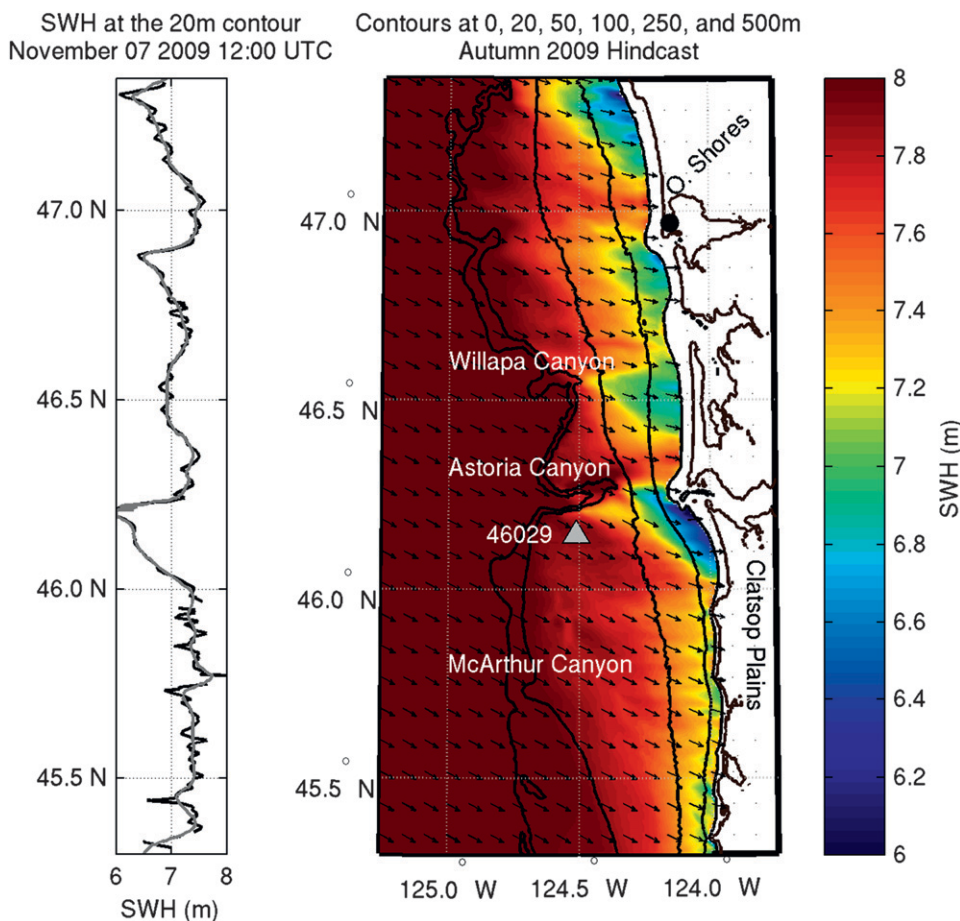


FIG. 9. As in Fig. 8, but for the hindcast in the northern OR and southwestern WA region. Large alongshore gradients in wave height are present at the 20-m contour. At buoy 46029, the modeled SWH was 7.9 m with an MWP of 16.4 s and PWD of 290°.

with the default wave breaking coefficient ($\gamma = 0.73$)—the same parameterization used in the WAVEWATCH implementation. The model was forced with alongshore-uniform conditions at the offshore boundary. The lateral boundaries (i.e., north and south) were extended 50 arc minutes (~ 92 km) to the north and to the south assuming straight and parallel contours, and a one-dimensional model run was executed at the top and bottom latitudes. As opposed to WAVEWATCH, which uses an explicit propagation scheme, SWAN solves Eq. (1) with an implicit second-order numerical scheme; this implementation uses the default for stationary computations (more details in Rogers et al. 2002). SWAN was executed in spherical coordinates over the same NearWW3_PNW shelf grids. A total of 24 logarithmically spaced frequency bins from 0.041 18 to 0.50 Hz were considered and the directional resolution was 5°. The SWAN default convergence criterion was applied, where the local or spatially averaged change in SWH

and MWP from successive iterations should be less than 2% over all wet points to stop computations. With this additional tool we investigate the conditions that lead to variability in the inner-shelf waves (at the 20-m contour) and also identify the responsible wave transformation process.

1) STONEWALL, HECETA, AND PERPETUA BANKS

In this section we will investigate under which conditions the Stonewall, Perpetua, and Heceta Banks affect the wave field at the 20-m isobath. The Stonewall Bank, located near Newport, reaches depths as shallow as 50 m at more than 20 km offshore. Southwest of the Stonewall Bank are the Perpetua and Heceta Banks, both with water depths as shallow as 80 m. According to linear wave theory, waves with periods larger than 10 s may be affected by these features. Two questions were of particular interest to us: determining which physical process is responsible for the predicted wave transformation and

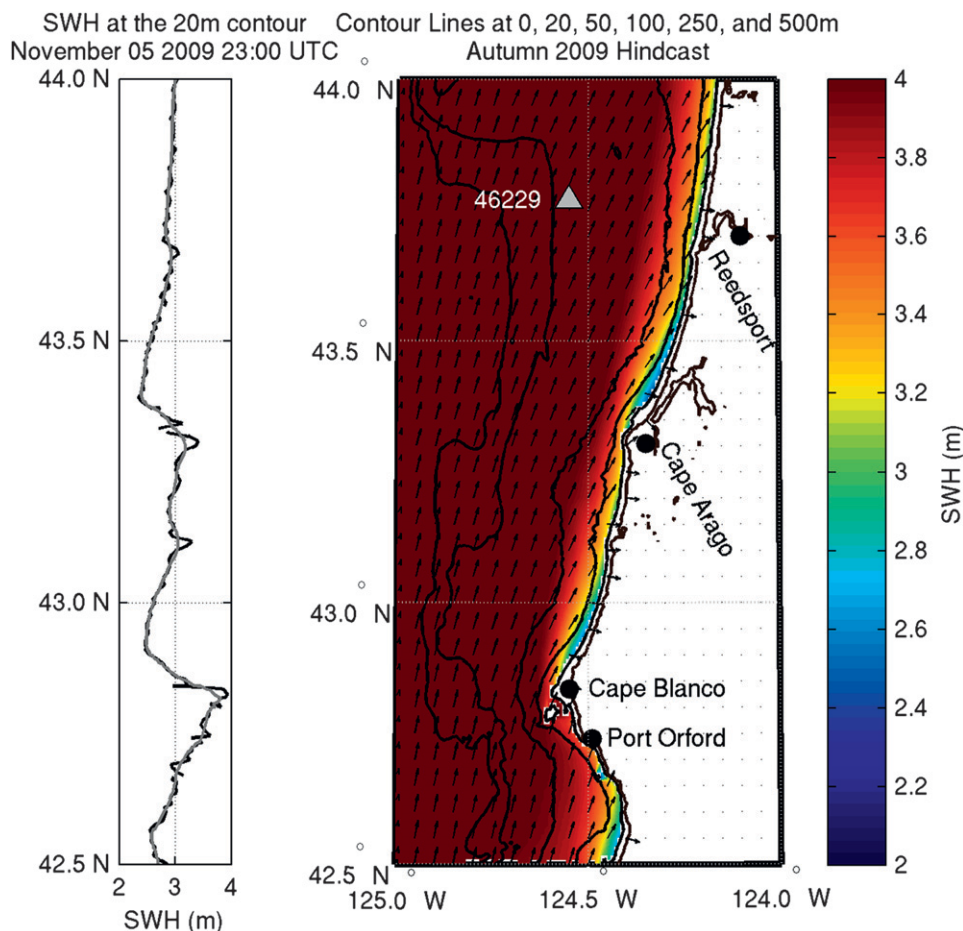


FIG. 10. As in Fig. 8, but for the hindcast in the southern OR region. Wave height reduction is observed north of both Cape Blanco and Cape Arago. At buoy 46229, the modeled SWH was 4.3 m with an MWP of 8.7 s and PWD of 209°.

documenting under which conditions the banks affect the nearshore waves.

To separate the effects of shoaling and refraction, three SWAN simulations were carried out including both two-dimensional refraction processes and shoaling (hence, the full model) in case A, only shoaling in case B, and shoaling along with a one-dimensional refraction⁴ formulation assuming straight and parallel contours in the east–west direction at the selected transect in case C (see Fig. 11). Note that differences between cases B and C identify modifications due to refraction that would occur even if focusing around the banks was not present. Differences between cases A and C highlight the focusing

effects of the banks. All simulations are forced by a 2D JONSWAP spectrum on all open boundaries. The spectrum used for each simulation was based on the hindcasted wave spectrum at buoy 46050 for 1200 UTC 7 November 2009 (corresponding to the case in Fig. 8). At this time the hindcasted spectral parameters were SWH of 7.6 m, PWP of 16.3 s, and PWD of 293°; the default peak enhancement parameter with a value of 3.3 and a directional spread of 12° were used. This is a rather large wave height; however, SWAN, in the configuration used here, is essentially a linear wave propagation model and, hence, results outside the surf zone are not sensitive to the absolute value of wave height.

The top panel in Fig. 11 shows transects of wave height at 44.5°N for the three aforementioned SWAN simulations. All three cases display the wave height decay entering intermediate water depths (124.7°W), indicating that the decay is due to the shoaling process associated with the localized increase in the group

⁴ This is in essence similar to performing a 1D SWAN simulation. We performed a 2D simulation with refraction on a grid where we replicate the cross section of interest a few times north and south, thus creating a 2D grid with straight and parallel contours.

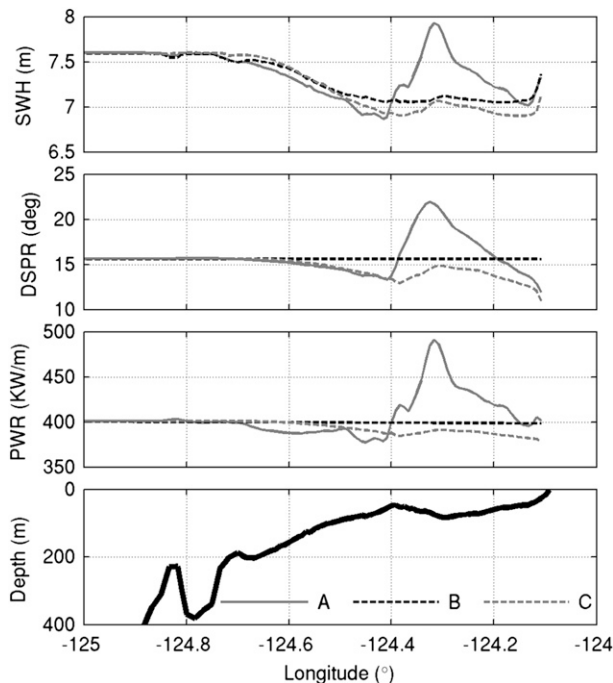


FIG. 11. Cross sections along 44.5°N from the SWAN simulations: (from top to bottom) SWH, DSPR, PWR, and local bathymetry. Case A includes wave refraction, case B neglects refraction, and case C includes refraction but the simulation was performed for straight and parallel contours on that transect. Results at water depths shallower than 20 m are masked out since they are not considered in the present discussion. JONSWAP spectral parameters are SWH, 7.6 m; PWP, 16.3 s; MWD, 293°; and directional spread of 12°.

velocity. The wave power ($PWR = Ec_g$) is not altered in the absence of refraction (see third panel in Fig. 11); therefore, an increase in group velocity is primarily responsible for the decrease in wave height. This can also be corroborated with an analysis of the shoaling coefficient (Dean and Dalrymple 1991) that indicates that for swell wave periods greater than 10 s the shoaling coefficient is less than unity for much of the domain contained within the bathymetric contours of 50–100 m. Note that the shoaling coefficient will increase to exceed unity in shallower water depths. This indicates that a large portion of the Oregon shelf is in transitional water depths where a decrease in wave height is related to a dip in the shoaling coefficient that is usually considered a brief phenomenon.

Case A, which includes refraction on alongshore varying bathymetry, shows increased wave height shoreward of the bank. This is the region of wave focusing due to refraction on the banks, since shoaling is not the dominant process the wave power increases in these locations. In the focusing region, an increase in the directional spreading (DSPR), as described in Kuik

et al. (1988), is expected because waves turn around the shoal into the focusing zone (see second panel in Fig. 11). Cases B and C, which do not include two-dimensional refraction, exhibit minor wave recovery shoreward of the bank due to deshoaling. Note that cases A and B predict a similar wave height just shoreward of 124.2°W, indicating that the effects of wave focusing are no longer apparent shoreward of this location.

To understand under which conditions the waves are amplified at the 20-m isobath, a series of simulations were performed with the same JONSWAP spectrum as before for multiple directions (ranging from 240° to 300°) and periods (ranging from 8 to 20 s). These series of simulations as well as those in the following sections will use the same JONSWAP peak enhancement parameter with a value of 3.3 to model the frequency spectrum, and the directional distribution is modeled with a cosine function with a directional spread of 20°. Example results for 250° wave incidence (corresponding to waves from the southwest) and 16.3-s waves (see Fig. 12) indicate a wave focusing area offshore of Newport, between 44.2° and 44.6°N. The rays in the plot show the focusing and defocusing regions in the shelf. Figure 13 shows a series of wave heights at 20-m water depth for different angles of incidence. When waves approach from the southwest (Fig. 11, left), the wave focusing becomes evident between 44.2° and 44.6°N. The position of this amplified zone is a function of the incidence angle; as waves approach more perpendicular to shore, the zone is displaced southward. When waves approach from the northwest, this amplified zone moves farther south, losing its intensity. This is related to the enhanced focusing effect when waves approach from the southwest (cf. Figs. 12 and 8) causing a larger focusing region that is still effective at the 20-m contour. In contrast, the focusing region for northwesterly wave incidence is wider but does not extend as far toward the shore. The magnitude of this amplification is correlated with the wave period (see Fig. 14). The longer wave periods produce greater alongshore variability for the same SWH and PWD. Hence, wave amplification in this zone is strongest for long waves coming from the southwest direction.

2) ASTORIA AND WILLAPA CANYONS

The Astoria Canyon is one of the most distinct features on the PNW shelf. The canyon's head is approximately 18 km west of the mouth of the Columbia River (MCR) where the approximate water depth is 100 m (*Encyclopaedia Britannica* 2012). Farther north, the Willapa Canyon heads at approximately 35 km west of Ocean Park, Washington. In contrast to banks, canyons divert wave energy but also, by the same physical process,

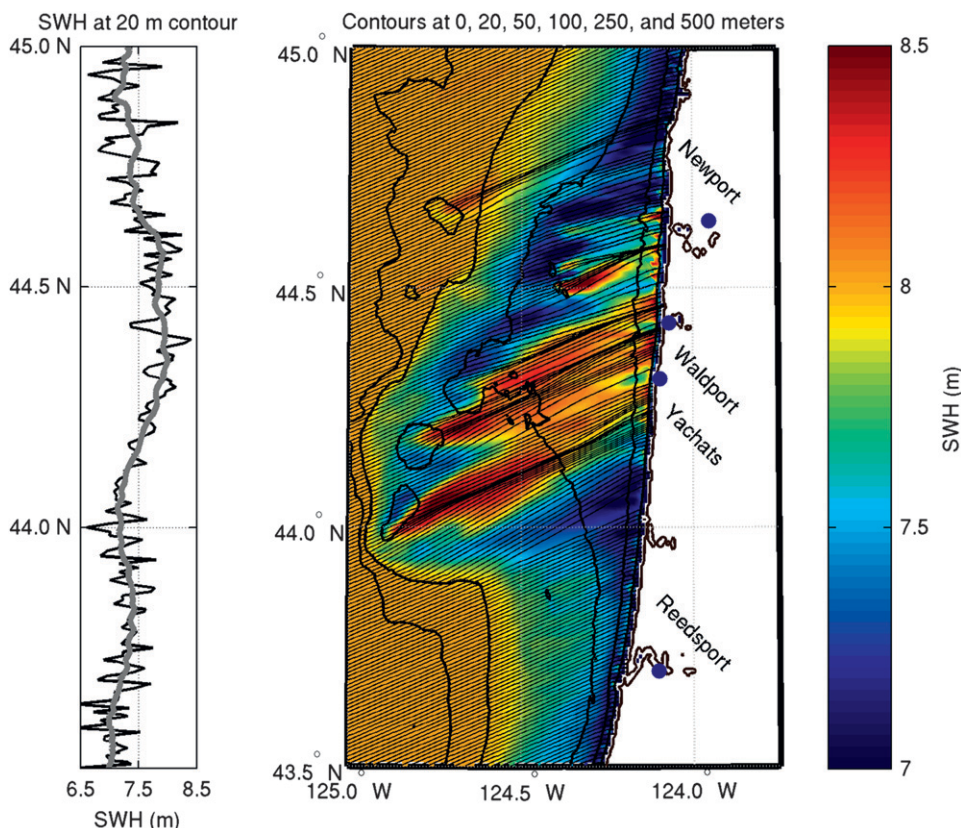


FIG. 12. (left) The significant wave height at the 20-m contour. The black and gray lines show raw model output (unsmoothed) and smoothed with a moving averaging, respectively. (right) The significant wave height in colors and wave rays over the modeling domain for a steady-state SWAN simulation. Wave heights are amplified near Waldport, OR. JONSWAP spectral parameters are SWH, 8 m; PWP, 16.3 s; and MWD, 250°.

refraction. Our interest is to determine whether the wave field at the 20-m isobath along the northern Oregon and southwest Washington coast shows large-scale variations due to the presence of the canyon. A series of SWAN simulations were performed based on the hindcasted conditions at 1200 UTC 7 November 2009 at buoy 46029 forced by a JONSWAP spectrum uniformly along the offshore boundary with SWH of 8 m, with multiple periods and directions.

Figure 15 shows a series of SWH plots at the 20-m isobath as a function of wave incident angle for 18-s waves. When waves approach from the southwest (Fig. 15, left), wave energy is diverted and a shadow zone appears in the southern part of the Long Beach Peninsula (labeled as LBP). This shadow zone lies south of an area where wave energy is concentrated. This energy concentration occurs because both the Willapa and Astoria Canyons divert wave energy. In the area between them, the diverted wave energy is concentrated. Similar patterns were also predicted for the Scripps and La Jolla Canyons in California [see, e.g., Long and

Özkan-Haller (2005) and Magne et al. (2007)]. This creates significant gradients in alongshore SWH; for example, when waves approach at 240°, the normalized wave height increases from 0.79 at 46.38°N to 1.05 at 46.51°N; this corresponds to a 25% difference in a distance of only 14 km. These gradients are produced by the presence of the canyons; otherwise, LBP has almost straight and parallel contours where this behavior would not be expected to occur. Since diffraction is not considered in these simulations, the gradients may be smaller in reality. However, Magne et al. (2007) found that refraction is the dominant process for swell transformation in Scripps Canyon, a similar study area also on the West Coast. When waves approach from the northwest (Fig. 15, middle) the gradients (at LBP) in wave height are still present but now the area offshore of the Clatsop Plains is sheltered. For the case when waves approach at 300°, the SWH may be smaller than 70% of the offshore SWH. This strong sheltering is based on a combination of the local bathymetry and the Astoria Canyon. The canyon diverts wave energy when the

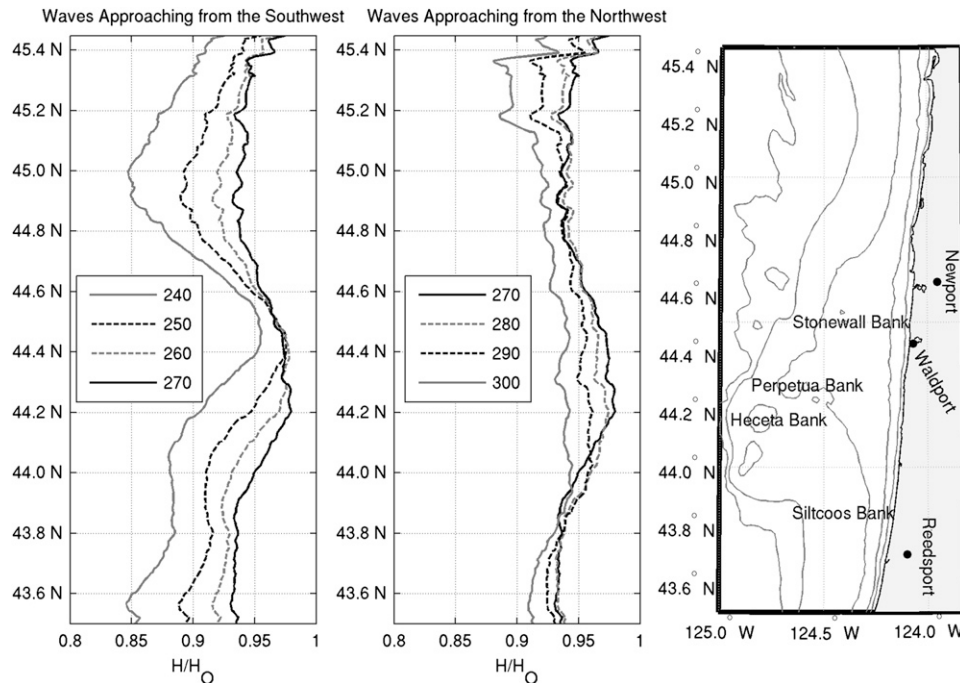


FIG. 13. Smoothed wave heights normalized by offshore SWH (H_0) for waves approaching from the (left) southwest and (middle) northwest at the 20-m isobath. The JONSWAP spectrum used for these SWAN simulations had an SWH of 8 m and a PWP of 16.3 s. (right) A map of the area considered in these simulations along with the features of interest. Contour lines are drawn at 20-, 50-, 100-, 150-, and 250-m water depths.

approach is from the northwest creating a shadow zone, which in combination with the concave-shaped depth contours (see right panel in Fig. 15) reduce the wave energy in the region.

The Willapa Canyon shelters the LBP when waves approach from the northwest (Fig. 15, middle), although to a lesser extent than the sheltering provided to this same area by the Astoria Canyon when waves approach from the southwest (Fig. 15, left). When waves approach from the northwest, Astoria Canyon diverts wave energy and shelters the Clatsop Plains (also see Fig. 9). Not only does the canyon reduce the waves in this region, but the inner-shelf bathymetry also contributes since the isobaths (Fig. 15, right) are concave shaped. As an example, when waves approach at 300° , their average offshore normalized wave height is 0.64 near the tip of the canyon at 46.20°N but exceeds 0.95 a distance 22.2 km south at 46.00°N . For wave incidence from the southwest, sharper wave height gradients exist on the northern side of the shadow regions than on the southern side. This is consistently the case for all the canyon shadows in the domain.

Figure 16 shows results from seven simulations with waves approaching at 300° . As expected, longer-period waves are affected to a larger extent, producing more

significant alongshore gradients at the 20-m isobath. For example, the wave height difference between 46.20° and 46.28°N (a distance of 8.9 km) is more than 15% as large for 20-s waves compared to the case involving 8-s waves. Nonetheless, even waves as short as 8 s still attain significant alongshore variability in the Clatsop Plains. Since at this wave period, the effect of the canyons is rather small; these are present due to the local concave-shaped contours, as suggested above. Therefore, it is expected that this zone experiences smaller waves than neighboring locations for a wide array of wave conditions from the northwest. Further sheltering is present for longer waves because these experience refraction on Astoria Canyon and from the inner-shelf bathymetry, both reducing the wave density.

3) CAPE BLANCO

Cape Blanco, located 10 km north of Port Orford, Oregon, is easily distinguishable as the westernmost location in the state. The orientation of the coastline changes appreciably at this location, and the coastline to the north of Cape Blanco faces toward the northwest by approximately 15 arc degrees (see Fig. 17). Cape Arago is another location where the shoreline orientation adjusts, and the beach to the north of Cape Arago faces

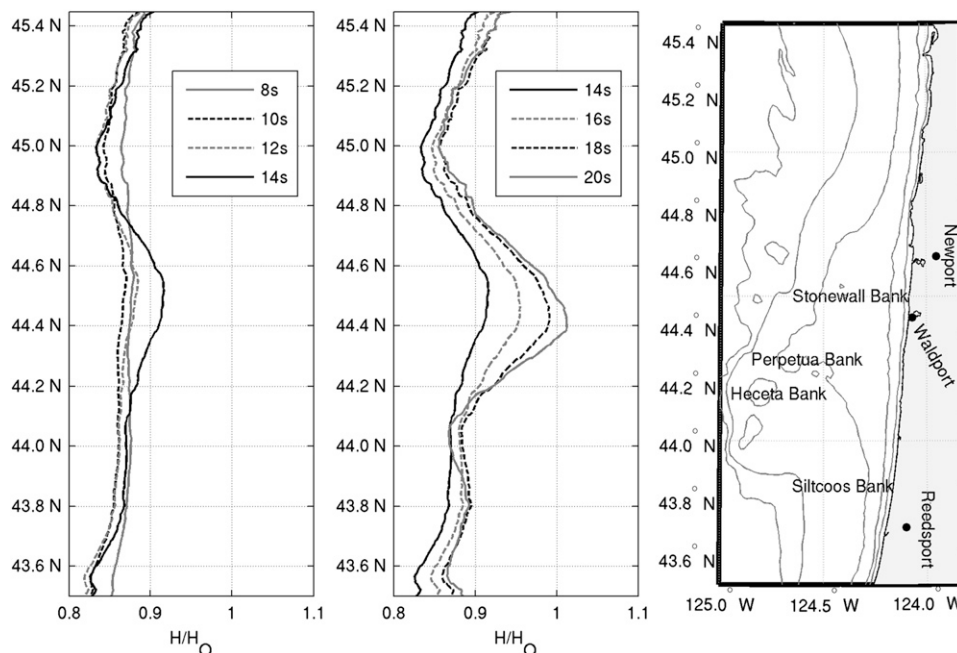


FIG. 14. As in Fig. 13, but for peak wave periods of (left) 8–14 s and (middle) 14–20 s at the 20-m isobath; wave height gradients are a function of PWP. The JONSWAP spectrum used for these SWAN simulations had an SHW of 8 m and a mean wave direction of 240°.

farther northwest. The bathymetry contours indicate two subtle large-scale embayments in this region: one between Cape Blanco and Cape Arago and one north of Cape Arago. Such embayments are expected to cause refraction patterns that divert the energy away from the middle of the embayment and focus energy near the edges (Long and Özkan-Haller 2005).

A series of SWAN simulations were performed in this region for varying wave incidence angles. Figure 17 shows SWH plotted at the 20-m isobath as a function of MWD. Results indicate that highly oblique incident waves from the south are affected by the presence of the capes and the associated bathymetric features. The effect is more pronounced for a more oblique angle of incidence. For example, at 42.95°N waves are more than 30% smaller for MWDs of 220° than for 270°. At these high incidence angles, the wave direction is almost parallel to the bathymetric contours just offshore of Cape Blanco and also of Cape Arago (see Fig. 10); hence, strong refraction has to occur. The reduced wave heights are a result of this process, although simulations neglecting refraction show that the shoaling mechanism identified as responsible for the gentle decline of the wave height on the shelf also plays a minor role here. The wave height patterns in Fig. 17 indicate a consistent picture. The wave height is severely reduced immediately to the north of each cape, creating a large local alongshore gradient in wave height. A milder wave

height increase then follows. The resulting pattern can be interpreted as wave sheltering due to the presence of the capes, similar to the sheltering caused by refraction around the banks or canyons.

Figure 18 shows SWH at the 20-m isobath as a function of wave period for a wave incidence of 220°. We find that the effect is relatively insensitive to wave period. This is because the bathymetric features associated with the capes are in water depths shallow enough to affect relatively short waves. Nonetheless, for PWP of 8 s the effect is somewhat reduced.

6. Conclusions

In this paper, we describe and assess the performance and implementation of a high-resolution wave forecasting model for the Oregon and southwest Washington coast. The performance assessment indicates an improvement in our ability to forecast inner-shelf wave conditions in comparison with existing operational forecasting models. This model excels in capturing the along-shore variability of the wave field when compared to current operational models by resolving the major bathymetric features on the continental shelf. WAVEWATCH III v3.14 proved to be skillful in intermediate to shallow waters in the PNW, with normalized errors in SWH and MWP on the order of 0.20 and 0.15, respectively. This model tends to overpredict the SWH and shows no

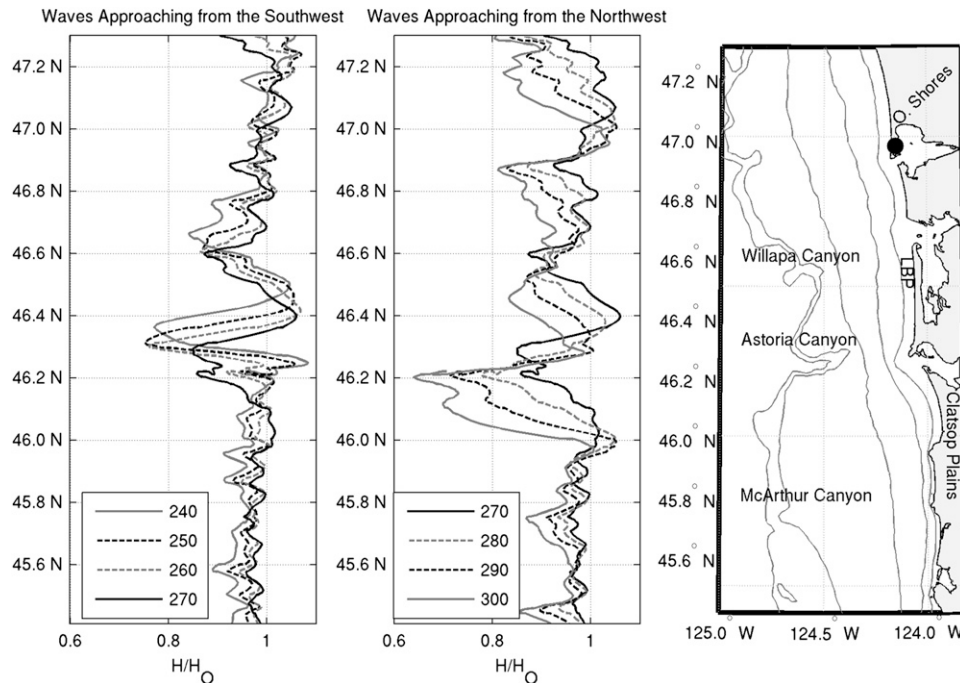


FIG. 15. As in Fig. 13, but for latitudes 45.6°–47.2°N. The JONSWAP spectrum used for these SWAN simulations had an SHW of 8 m and a mean wave period of 18 s.

seasonal fluctuations when considering normalized errors in significant wave height. Having a dedicated wave forecasting system at this coast provides the flexibility to output wave data where stakeholders, recreational

users, and people interested in wave energy need it. The forecasts are available online at no cost to the user via the Northwest Association of Networked Ocean Observing Systems (NANOOS) Visualization System

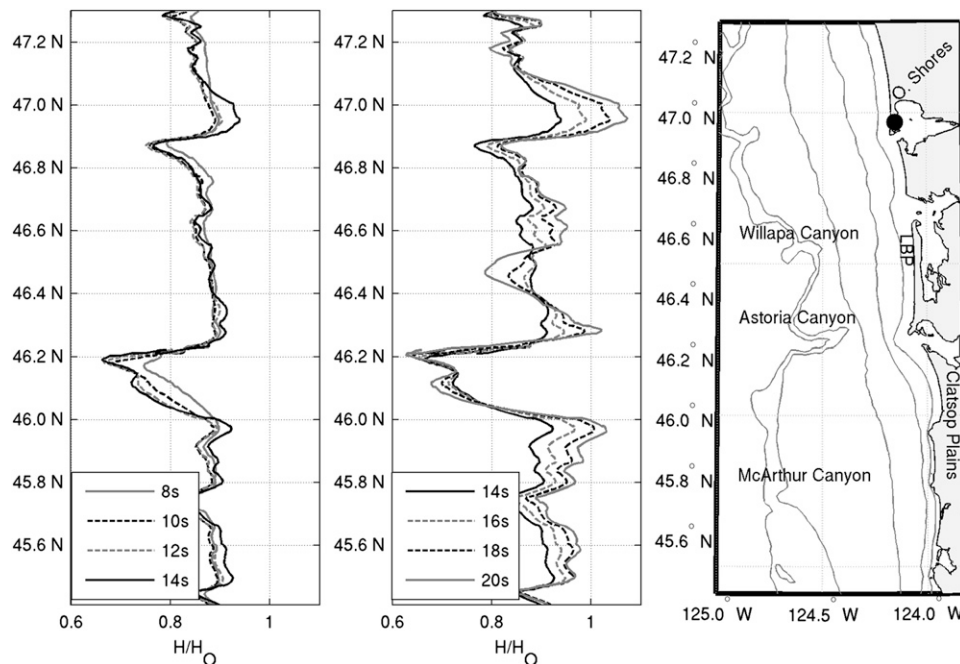


FIG. 16. As in Fig. 14, but for latitudes 45.6°–47.2°N. The JONSWAP spectrum used for these SWAN simulations had an SHW of 8 m and a mean wave direction of 300°.

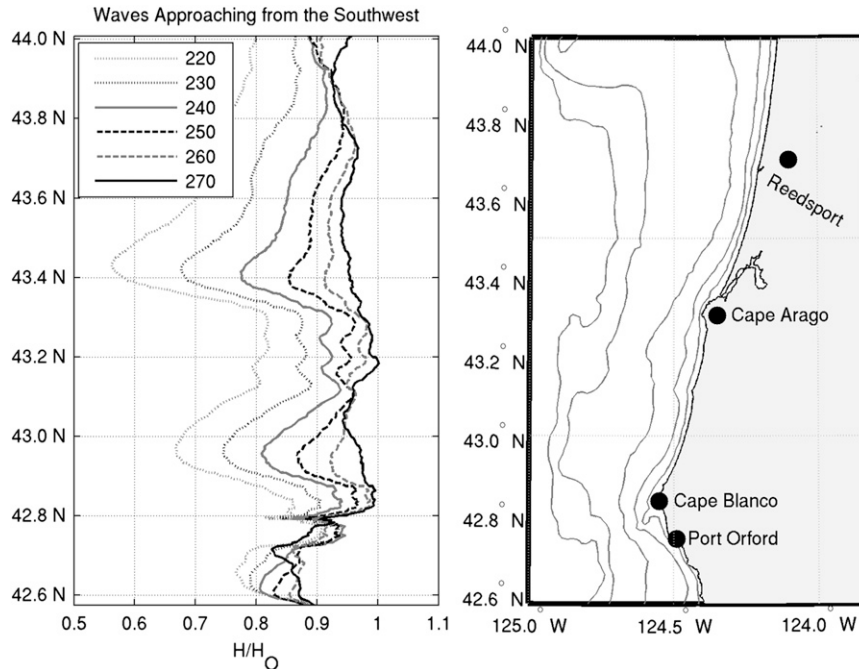


FIG. 17. As in Fig. 13, but only for directions of 220°–270° and for latitudes 42.6°–44.0°N.

(NVS) interface (Risien et al. 2009). At the time of this writing we are providing spatial plots of SWH, PWD, and PWP for each forecast hour in addition to spectral and bulk parameter data at 233 locations with a 2-km resolution along our domain at the 25-m contour.

The Stonewall, Perpetua, and Heceta Banks; the Astoria and McArthur Canyons; and Capes Blanco and Arago are bathymetric features that are shown to be

capable of producing alongshore variability in wave height in this region. For the bank systems, we find a wave amplification zone near Newport for waves approaching from the southwest. The amplification zone occurs farther south for more normal wave incidence and disappears for waves from the northwest. For the canyons systems, we find several focusing and defocusing areas. Their locations are highly sensitive to the wave

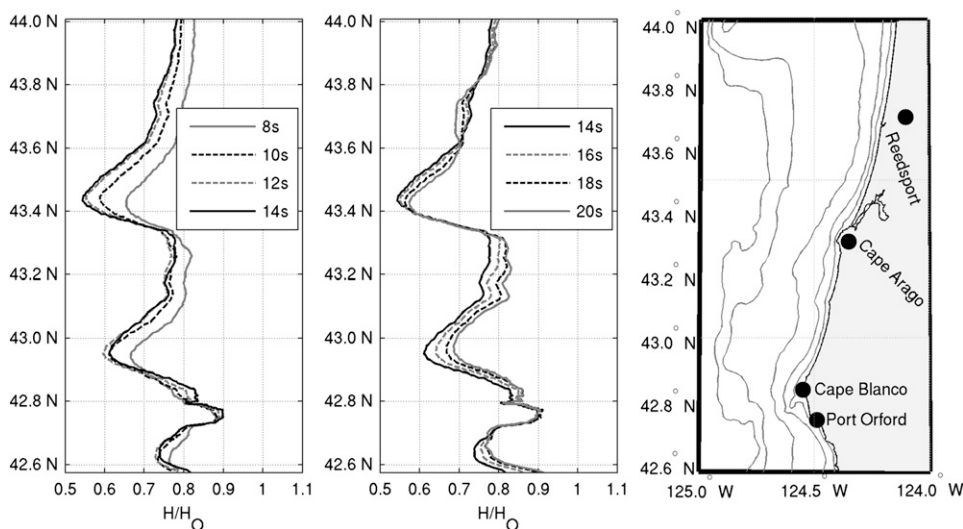


FIG. 18. As in Fig. 14, but for latitudes 42.6°–44.0°N. The JONSWAP spectrum used for these SWAN simulations had an SHW of 8 m and a PWD of 220°.

incidence angle, although they exist for waves from any angle. Locally, large wave height gradients are generated near the edges of the sheltering zones. Finally, we find that Cape Blanco and Cape Arago are associated with a change in orientation of the bathymetric contours. This gives rise to locally large incidence angles and induces significant wave refraction, resulting in a sheltering zone to the north of the canyons for large incidence angles from the southwest. Note that such highly oblique waves from the southwest are not uncommon (see Fig. 2) but waves do not tend to approach at similar incidence angles from the northwest.

The magnitude of the effects for the banks, canyons, and capes is a function of the wave period, though more so for the bank systems where the focusing effect is no longer discernible for waves with periods less than 10 s. In contrast, for the canyons and capes the sheltering or focusing effects are still evident even for waves as short as 8 s, albeit with a reduced magnitude. This is related to the shallower area of influence of the canyons (that protrude shoreward to the 100-m contour) and the capes (that are most effective at the shallowest depths).

We note that wave height in water depths $50 < h < 100$ m was consistently less energetic compared to the offshore wave field. We find that this is not related to wave dissipation processes (such as bottom friction, whitecapping, or wave breaking) but, rather, it is controlled by wave shoaling on the continental shelf. Our sensitivity analyses show that neither bottom friction nor wind growth affect the model performance when considering bulk wave parameters at the shelf scale for wave forecasting–hindcasting in the PNW. Wave-shoaling processes cause a reduction in the wave height from the outer edge of the continental shelf to the inner shelf. This is related to the associated slight increase in the group velocity of the waves predicted by linear wave kinematics. Hence, we find that a large part of the Oregon shelf is characterized by transitional water depths for the dominant wave periods.

Acknowledgments. We wish to thank NANOOS for their contributions in the data dissemination. We also thank the investigators who obtained the observations used for the data–model comparisons. In particular, Jack Barth, Anthony Kirincich, Ata Suanda, and their field crew obtained the RP09 and NP05 datasets. The RP09 data collection was funded by the Oregon Wave Energy Trust (OWET); the NP05 was gathered through the Partnership for Interdisciplinary Studies of Coastal Oceans (PISCO), funded primarily by the Gordon and Betty Moore Foundation and the David and Lucile Packard Foundation. We thank the Department of the Interior’s United States Geological Survey and the

Washington State Department of Ecology for providing the GH99 data. Also, we thank NOAA’s National Weather Service for providing the WAVEWATCH III source code and colleagues Sarah Kassem and Gregory Wilson for helpful discussions.

The work presented in this paper was supported by Oregon Sea Grant under Award NA10OAR4170059 and by the Department of Energy under Award DE-FG36-08GO18179. Neither the U.S. government nor any agency thereof, nor any of their employees, makes any warranty, expressed or implied, or assumes any legal liability or responsibility for the accuracy, completeness, or usefulness of any information, apparatus, produce, or process disclosed, or represents that its use would not infringe upon privately owned rights. Reference herein to any specific commercial product, process, or service by trade name, trademark, manufacturer, or otherwise does not necessarily constitute or imply its endorsement, recommendation, or favoring by the U.S. government or any agency thereof. The views and opinions of the authors expressed herein do not necessarily state or reflect those of the U.S. government or any agency thereof.

APPENDIX

Statistical Metrics

In the following statistical metrics, N represents the number of observations, while MEAS and EST are the measured and modeled values, respectively. These metrics are root-mean-squared error (RMSE),

$$\text{RMSE} = \sqrt{\frac{\sum (\text{MEAS}_i - \text{EST}_i)^2}{N}}; \quad (\text{A1})$$

normalized root-mean-squared error (NRMSE),

$$\text{NRMSE} = \sqrt{\frac{1}{N} \sum \left(\frac{\text{MEAS}_i - \text{EST}_i}{\text{MEAS}_i} \right)^2}, \quad (\text{A2})$$

where the NRMSE is analogous to the operational performance index in Ris et al. (1999); and the scatter index (SI),

$$\text{SI} = \frac{\text{RMSE}}{\overline{\text{MEAS}}}, \quad (\text{A3})$$

as described by Ris et al. (1999) and Romeiser (1993), among others. Other metrics used to characterize the model performance are the bias,

$$\text{Bias} = \frac{1}{N} \sum (\text{EST}_i - \text{MEAS}_i), \quad (\text{A4})$$

and the linear correlation coefficient (r^2)

$$r^2 = \frac{[\sum(\text{MEAS}_i - \overline{\text{MEAS}})(\text{EST}_i - \overline{\text{EST}})]^2}{\sqrt{[\sum(\text{MEAS}_i - \overline{\text{MEAS}})^2][\sum(\text{EST}_i - \overline{\text{EST}})^2]}} \quad (\text{A5})$$

A perfect model run with respect to measured data will report an RMSE, NRMSE, SI, and bias of zero and a linear correlation coefficient of 1. These statistics are computed only where the data and model coincide in time allowing for a 10-min offset.

REFERENCES

- Allan, J. C., and P. D. Komar, 2000: Are ocean wave heights increasing in the eastern North Pacific? *Eos, Trans. Amer. Geophys. Union*, **81**, 561–567.
- , and —, 2002: Extreme storms on the Pacific Northwest coast during the 1997–98 El Niño and 1998–99 La Niña. *J. Coastal Res.*, **18**, 175–193.
- , and —, 2006: Climate controls on US West Coast erosion processes. *J. Coastal Res.*, **223**, 511–529.
- Alvarez-Ellacuria, A., A. Orfila, M. Olabarrieta, R. Medina, G. Vizoso, and J. Tintoré, 2010: A nearshore wave and current operational forecasting system. *J. Coastal Res.*, **263**, 503–509.
- Amante, C., and B. W. Eakins, 2009: ETOPO1 1 arc-minute global relief model: Procedures, data sources and analysis. NOAA Tech. Memo. NESDIS NGDC-24, 19 pp.
- Arinaga, R. A., and K. F. Cheung, 2012: Atlas of global wave energy from 10 years of reanalysis and hindcast data. *Renewable Energy*, **39**, 49–64.
- Battjes, J. A., and J. P. F. M. Janssen, 1978: Energy loss and set-up due to breaking of random waves. *Proc. 16th Int. Conf. on Coastal Engineering*, Hamburg, Germany, ASCE, 569–587.
- Booij, N., and L. H. Holthuijsen, 1987: Propagation of ocean waves in discrete spectral wave models. *J. Comput. Phys.*, **68**, 307–326.
- , R. C. Ris, and L. H. Holthuijsen, 1999: A third-generation wave model for coastal regions: 1. Model description and validation. *J. Geophys. Res.*, **104** (C4), 7649–7666.
- Carignan, K. S., L. A. Taylor, B. W. Eakins, and R. R. Warnken, 2009a: Digital elevation model of Astoria, Oregon: Procedures, data sources and analysis. NOAA Tech. Memo. NESDIS NGDC-22, National Geophysical Data Center, Boulder, CO, 44 pp.
- , —, —, —, E. Lim, and P. Grothe, 2009b: Digital elevation model of central Oregon coast: Procedures, data sources and analysis. NOAA Tech. Memo. NESDIS NGDC-25, National Geophysical Data Center, Boulder, CO, 46 pp.
- , —, —, —, T. Sazonova, and D. C. Schoolcraft, 2009c: Digital elevation model of Garibaldi, Oregon: Procedures, data sources and analysis. NOAA Tech. Memo. NESDIS NGDC-16, National Geophysical Data Center, Boulder, CO, 26 pp.
- , —, —, —, —, and —, 2009d: Digital elevation model of Port Orford, Oregon: Procedures, data sources and analysis. NOAA Tech. Memo. NESDIS NGDC-21, National Geophysical Data Center, Boulder, CO, 34 pp.
- Christensen, A., S. Rowe, and M. D. Needham, 2007: Value orientations, awareness of consequences, and participation in a whale watching education program in Oregon. *Hum. Dimensions. Wildl.*, **12**, 289–293.
- Cornett, A. M., 2009: A global wave energy resource assessment. *Sea Technol.*, **50**, 59–64.
- Dean, R. G., and R. A. Dalrymple, 1991: *Water Wave Mechanics for Engineers and Scientists*. Advanced Series on Ocean Engineering, Vol. 2, World Scientific, 353 pp.
- Encyclopaedia Britannica*, cited 2012: Astoria Canyon. [Available online at <http://www.britannica.com/EBchecked/topic/39897/Astoria-Canyon>.]
- Environmental Modeling Center, 2003: The GFS atmospheric model. NCEP Office Note 442, 14 pp.
- Falcão, A. F. O., 2010: Wave energy utilization: A review of the technologies. *Renewable Sustainable Energy Rev.*, **14**, 899–918.
- Folley, M., and T. Whittaker, 2009: Analysis of the nearshore wave energy resource. *Renewable Energy*, **34**, 1709–1715.
- Gelfenbaum, G., C. R. Sherwood, L. A. Kerr, and K. Kurrus, 2000: Grays Harbor wave refraction experiment 1999: Data report. USGS Open-File Rep. 00–404, 132 pp. [Available online <http://pubs.usgs.gov/of/2000/of00-404/>.]
- Gemmrich, J., B. Thomas, and R. Bouchard, 2011: Observational changes and trends in northeast Pacific wave records. *Geophys. Res. Lett.*, **38**, L22601, doi:10.1029/2011GL049518.
- Gorrell, L., B. Raubenheimer, S. Elgar, and R. Guza, 2011: SWAN predictions of waves observed in shallow water onshore of complex bathymetry. *Coastal Eng.*, **58**, 510–516.
- Grothe, P., L. A. Taylor, B. W. Eakins, K. S. Carignan, R. R. Warnken, E. Lim, and R. J. Caldwell, 2010: Digital elevation model of Taholah, Washington: Procedures, data sources and analysis. NOAA Tech. Memo. NESDIS NGDC-34, National Geophysical Data Center, Boulder, CO, 28 pp.
- , —, —, —, R. J. Caldwell, E. Lim, and D. Z. Friday, 2011: Digital elevation model of Crescent City, California: Procedures, data sources and analysis. NOAA Tech. Memo. NESDIS NGDC-51, National Geophysical Data Center, Boulder, CO, 31 pp.
- Hanson, J. L., B. A. Tracy, H. L. Tolman, and R. D. Scott, 2009: Pacific hindcast performance of three numerical wave models. *J. Atmos. Oceanic Technol.*, **26**, 1614–1633.
- Hasselmann, K., and Coauthors, 1973: Measurements of wind-wave growth and swell decay during the Joint North Sea Wave Project (JONSWAP). Deutsches Hydrographisches Institut Rep. A(8) (No. 12), 95 pp.
- Hasselmann, S., K. Hasselmann, J. H. Allender, and T. P. Barnett, 1985: Computations and parameterizations of the nonlinear energy transfer in a gravity-wave spectrum. Part II: Parameterizations of the nonlinear energy transfer for application in wave models. *J. Phys. Oceanogr.*, **15**, 1378–1391.
- Iversen, H. W., 1952: Waves and breakers in shoaling water. *Proc. Third Conf. on Coastal Engineering*, Cambridge, MA, Council on Wave Research, 1–12.
- Kirincich, A. R., S. J. Lentz, and J. A. Barth, 2009: Wave-driven inner-shelf motions on the Oregon coast. *J. Phys. Oceanogr.*, **39**, 2942–2956.
- Komar, P. D., J. C. Allan, and P. Ruggiero, 2009: Ocean wave climates: Trends and variations due to Earth's changing climate. *Handbook of Coastal and Ocean Engineering*, Y. C. Kim, Ed., World Scientific Publishing, 971–975.
- Kuij, A. J., G. P. van Vledder, and L. H. Holthuijsen, 1988: A method for the routine analysis of pitch-and-roll buoy wave data. *J. Phys. Oceanogr.*, **18**, 1020–1034.
- Long, J. W., and H. T. Ozkan-Haller, 2005: Offshore controls on nearshore rip currents. *J. Geophys. Res.*, **110**, C12007, doi:10.1029/2005JC003018.

- Magne, R., K. A. Belibassakis, T. H. C. Herbers, F. Ardhuin, W. C. O'Reilly, and V. Rey, 2007: Evolution of surface gravity waves over a submarine canyon. *J. Geophys. Res.*, **112**, C01002, doi:10.1029/2005JC003035.
- Menéndez, M., F. J. Méndez, I. J. Losada, and N. E. Graham, 2008: Variability of extreme wave heights in the northeast Pacific Ocean based on buoy measurements. *Geophys. Res. Lett.*, **35**, L22607, doi:10.1029/2008GL035394.
- NDBC, 2009: Handbook of automated data quality control checks and procedures. NDBC Tech. Doc. 09-02, NOAA/National Data Buoy Center, 78 pp.
- Rao, S., and S. Mandal, 2005: Hindcasting of storm waves using neural networks. *Ocean Eng.*, **32**, 667–684.
- Ris, R. C., L. H. Holthuijsen, and N. Booij, 1999: A third-generation wave model for coastal regions: 2. Verification. *J. Geophys. Res.*, **104** (C4), 7667–7681.
- Risien, C., and Coauthors, 2009: The NANOOS visualization system: Aggregating, displaying and serving data. *OCEANS 2009—Marine Technology for Our Future: Global and Local Challenges*, Biloxi, MS, MTS/IEEE, 1–9.
- Rogers, W. E., J. Kaihatu, H. Petit, N. Booij, and L. Holthuijsen, 2002: Diffusion reduction in an arbitrary scale third generation wind wave model. *Ocean Eng.*, **29**, 1357–1390.
- , —, L. Hsu, R. E. Jensen, J. D. Dykes, and K. T. Holland, 2007: Forecasting and hindcasting waves with the SWAN model in the Southern California Bight. *Coastal Eng.*, **54** (1), 1–15.
- Romeiser, R., 1993: Global validation of the wave model WAM over a one-year period using Geosat wave height data. *J. Geophys. Res.*, **98** (C3), 4713–4726.
- Ruggiero, P., P. D. Komar, and J. C. Allan, 2010: Increasing wave heights and extreme value projections: The wave climate of the U.S. Pacific Northwest. *Coastal Eng.*, **57**, 539–552.
- Sela, J. G., 1980: Spectral modeling at the National Meteorological Center. *Mon. Wea. Rev.*, **108**, 1279–1292.
- Seymour, R. J., 2011: Evidence for changes to the northeast Pacific wave climate. *J. Coastal Res.*, **27**, 194–201.
- Stockdon, H. F., R. A. Holman, P. A. Howd, and A. H. Sallenger Jr., 2006: Empirical parameterization of setup, swash, and runup. *Coastal Eng.*, **53**, 573–588.
- SWAN Team, 2010: SWAN user manual: SWAN cycle III version 40.91A. Delft University of Technology, 121 pp. [Available online at <http://swanmodel.sourceforge.net/>.]
- Tolman, H. L., 2002a: Alleviating the garden sprinkler effect in wind wave models. *Ocean Modell.*, **4**, 269–289.
- , 2002b: Validation of WAVEWATCH III version 1.15 for a global domain. NOAA/NWS/NCEP/OMB Rep. 213, 33 pp.
- , 2006: Development of a multi-grid version of WAVEWATCH III. NOAA/NWS/NCEP/MMAB Tech. Rep. 256, 88 pp.
- , 2008: A mosaic approach to wind wave modeling. *Ocean Modell.*, **25**, 35–47.
- , and D. Chalikov, 1996: Source terms in a third-generation wind wave model. *J. Phys. Oceanogr.*, **26**, 2497–2518.
- Young, I. R., S. Zieger, and A. V. Babanin, 2011: Global trends in wind speed and wave height. *Science*, **332**, 451–455.